JVST A
Journal of Vacuum Science & Technology A

ARTICLE

pubs.aip.org/avs/jva

# Consequences of secondary electron emission on charging of $SiO_2$ features in capacitively coupled plasmas having sinusoidal and tailored bias waveforms

Cite as: J. Vac. Sci. Technol. A 44, 023013 (2026); doi: 10.1116/6.0005187
Submitted: 25 November 2025 · Accepted: 20 January 2026 ·
Published Online: 18 February 2026



Chenyao Huang[1,a)] and Mark J. Kushner[2,b)]

## AFFILIATIONS

[1]Chemical Engineering Department, University of Michigan, 1301 Beal Ave., Ann Arbor, Michigan 48109-2122
[2]Electrical Engineering and Computer Science Department, University of Michigan, 1301 Beal Ave., Ann Arbor, Michigan 48109-2122

[a)]chenyaoh@umich.edu
[b)]**Author to whom correspondence should be addressed:** mjkush@umich.edu



## ABSTRACT

In plasma etching of dielectric materials for microelectronics fabrication, energetic ions with narrow angular distributions preferentially positively charge the bottom of features, while isotropic electrons preferentially charge the top negatively. This process generates intrafeature electric fields that can distort the trajectories of charged particles leading to defects. Remedies to alleviate charging include using voltage-waveform tailoring (VWT) to produce electron fluxes having higher energies and narrower angular distributions to better neutralize positive charge. One phenomenon relevant to the charging process is secondary electron emission (SEE), in which one or more electrons are emitted upon particle impact. In this work, we computationally investigated the dynamics of charging of high aspect ratio features in capacitively coupled plasmas sustained in argon. Charging of preformed features is discussed to better disconnect the evolution of the feature from charging dynamics. We found that SEE redistributes charge within the feature, lowering the in-feature positive electric potential and altering the electric potential profile. The reduction in potential is largest when the degree of SEE is the highest. The effectiveness of VWT to increase electron energies and narrow angular distributions in remediating charging was also investigated. We found that when including SEE, anisotropic electrons become less able to remediate charging as the potential in the feature is dominated by charge redistribution.



## I. INTRODUCTION

In addition to shrinking dimensions, semiconductor device manufacturing has adopted three-dimensional (3D) architectures to increase the areal device density. For example, the manufacture of 3D-NAND memory now begins with hundreds of alternating layers of silicon dioxide and silicon nitride (ONO) through which vias are etched using plasma processing techniques. Leveraging the anisotropic ion trajectories enabled by accelerating ions through wafer-bounding sheaths, vias having aspect ratios (ARs) approaching 100 can be fabricated. Typical dimensions of these vias are 30–100 nm in diameter and up to 10 $\mu$m deep.[1–3]

The increasing AR of these features presents several challenges for plasma etching.[4] One of the major challenges is the electrical charging of the features. During plasma etching, positive ions generally have nearly normal trajectories onto the wafer with energies exceeding several keV and so are able to penetrate deeply into the feature before colliding with the sidewalls. Ions striking surfaces will generally neutralize leaving the surface more positively charged. (The resulting energetic neutral particles are referred to here as *hot neutrals*.) Electrons generally arrive at the surface of the wafer with lower energies (several eV) and isotropic trajectories. These conditions result in net positive charge accumulation on surfaces deep within the feature (walls and bottom) and net negative

charge accumulation on surfaces near the top of the surface. This differential distribution of positive and negative charges then generates intrafeature electric fields, which can distort the trajectories of incoming ions, resulting in defects such as bowing, twisting, and notching, often also depending on the pattern of the features.[5,6] The propensity for charged induced distortions increases as the feature AR increases.[5–7]

When using capacitive coupling for bias power, the charged particle current to the wafer and charged particle fluxes to any point on a dielectric surface must be zero averaged over the AC period.[8] This is a similar requirement to an electrically floating surface in a low temperature plasma (LTP). For an isolated surface in the midst of a LTP where the electron temperature is higher than that for ions and electrons are more mobile than ions, this zero-current requirement is achieved by the surface charging negative producing a negative electrical potential.[8] This negative potential retards the flux of electrons while enhancing the flux of ions to the point that these fluxes electrically balance onto the surface. In charging of HAR features, the roles of electrons and ions are reversed. The ions arrive with higher energy and functionally have a higher mobility within the feature compared to electrons. The positive charging of the feature decreases the ion energy (turning back critically low-energy ions) while accelerating electrons into the feature. The final charging configuration achieves a balance between the fluxes of positive ions and electrons to all points within the feature in the steady state. The final positive potential will be less than the maximum ion energy due to the acceleration of electrons into the feature, an outcome that is necessary in order for etching to proceed.

With increasing AR comes aspect ratio dependent etching (ARDE), the phenomenon of the etch rate decreasing as AR increases.[6,9–11] The origins of ARDE include glancing collisions of ions (and hot neutrals) on the sidewalls of the feature prior to reaching the etch front at the bottom of the feature, which decreases their energy and so decreases their etch yield. A second cause of ARDE is the buildup of positive potential in the feature due to charging, producing electric fields that slow incoming ions and so decrease their etch yield. With increasing AR, the ion energy should be higher and angular distribution should be narrower in order to minimize ARDE. This is accomplished by increasing the radio frequency (RF) bias power by increasing the voltage amplitude, operating with lower sinusoidal frequency biases or using nonsinusoidal voltage waveforms.[12,13]

These strategies are designed to overcome charging as opposed to remediating charging. Strategies have also been investigated with the intent of mitigating charging. Pulsing the bias power consists of alternating periods of high bias power and low (or no) bias power. With pulsed periods having durations less than the RC time constant for charging, a lower positive potential in the feature is produced by lowering the incident average ion energy.[14] In neutral-beam etching, anisotropic fluxes of high-energy neutral particles are generated by neutralizing energetic ions, typically with a grid placed above the wafer so that charging of the feature can be minimized.[4,15] Combining pulsing the source power for the plasma with a highly thermally attaching electronegative gas results in electron attachment in the afterglow, producing an ion-ion plasma. In an ion-ion plasma, negative ions are no longer confined in the bulk plasma and are able to diffuse toward the wafer, where they can be accelerated into the feature to neutralize positive charge.[16] Use of a nonsinusoidal bias can generate electric field reversals adjacent to the wafer, accelerating electrons into features with high energies and narrow angular distributions, which works toward remediating positive charging.[8]

A better understanding of the dynamics of feature charging would aid efforts to design plasma equipment for processes that are less susceptible to the detrimental effects of charging. Matsui *et al.* employed a Monte Carlo simulation to investigate the time-evolution of electric potential in a trench in $SiO_2$ focusing on the conductivity of surface layers.[5] Using a mono-energetic ion beam with normal incidence, they demonstrated a correlation between AR and electric potential.[5] Ohmori *et al.* conducted *in situ* measurements of the electric potential at the bottom of poly-Si trenches having a $SiO_2$ bottom. They showed that the positive in-feature potential scales with AR and bias amplitude.[17] Jinnai *et al.* investigated the feature charging of $SiO_2$ vias to determine the consequences of the deposition of conductive polymer.[18] They showed an oscillation in electric potential when pulsing. Zhai *et al.* studied the degree of charging on hard masks and the effect on particle trajectories using a 3D simulation.[19] These research efforts highlight the importance of feature-scale charging dynamics.

Secondary electron emission (SEE) refers to the emission of one or more electrons, secondary electrons (SEs), when the surface undergoes particle bombardment. The incident particles may include ions, electrons, photons, excited atomic or molecular states, and hot neutrals.[20–27] The emission of electrons from surfaces is, from a current perspective, equivalent to positive ions incident onto the surface and so can lead to additional positive charging of the surface. Once emitted within a feature, SEs are accelerated by electric fields produced by previous charging. An SE emitted from one location striking another surface location in the feature can then reduce positive potential at the second location. Depending on the charging configuration of the feature, the SE can also escape from the feature. This transfer of charge within the feature with SEE results in a more dynamic transient phase during charging compared to the absence of SEE. These dynamics ultimately change the charging configuration and potential (magnitude and spatial distribution) in the feature. For example, Palov *et al.* investigated the consequences of SEE on trench charging, electric potential distribution, and ion energies using a three-dimensional (3D) Monte Carlo model and showed that the positive electric potential inversely scales with the degree of SEE.[23] The ion energy incident onto the bottom of the trench then increases due to the lower positive electric potential.[23]

In this paper, we discuss the results from a computational investigation of the consequences of secondary electron emission inside the feature on charging of HAR features for operating conditions that are typically used for the plasma etching of HAR features. These conditions are multiple-frequency capacitively coupled plasmas (CCPs) using sinusoidal and nonsinusoidal waveforms. To isolate the geometric effects of SEE from changes in the morphology of the feature that occurs during plasma etching, this work is focused on the dynamics and steady-state phases of charging of *preformed* trenches and vias in $SiO_2$ having varying AR. We discuss the relationship between the electric potential profile and SEE, the

relative contributions of ions and electrons to SEE, evaluate differences in charging due to geometry, and quantify the effect on the charging of using nonsinusoidal waveforms to accelerate electrons into the feature.

We found that the positive electric potential in the feature scales proportionally with ion energy and AR, both with and without SEE, although the spatial distribution of charge and the magnitude of charging are sensitive to SEE. The primary sources of SEE for our conditions are secondary emission by electrons, as their secondary-emission yield (SEY) can be several times greater than that of ions having energies less than several keV. When SEE is included, SEs serve as an additional charge-transfer process that reconfigures the charge distribution, which generally lowers the electric potential.

The model used for reactor-scale simulation and the reactor setup are described in Sec. II. The feature-scale simulation and SEE algorithms are discussed in Sec. III. Reactor-scale plasma properties and wafer-averaged energy-angular distributions (EADs) for electrons and ions are presented in Sec. IV. The relationship between electric potential and reactor conditions, the contributions of ions and electrons to SEE, and the consequences of geometry (AR, trench or via) on charging are discussed in Sec. V. The effectiveness of nonsinusoidal waveforms (voltage-waveform tailoring) in remediating charging with and without SEE are also discussed in Sec. V. Concluding remarks are in Sec. VI.

## II. DESCRIPTION OF THE REACTOR-SCALE MODEL

The modeling of reactor-scale plasma dynamics was performed using the Hybrid Plasma Equipment Model (HPEM).[28] The HPEM calculates reactor-scale plasma properties, including fluxes of charged particles to surfaces and their EADs. These fluxes to the wafer and their EADs are used as input to the Monte Carlo Feature Profile Model (MCFPM), which simulates the etching (not used here) and charging process of the feature.

A brief description of the options of HPEM used in this investigation is presented here while more detailed descriptions can be found in Refs. 8 and 28–30. The HPEM is a multifluid 2-dimensional simulator that contains modules which address different classes of physics involved in the plasma generation and transport processes. These modules exchange data in an iterative manner as the simulation (time integration) proceeds. Brief descriptions of the modules used in this investigation follow. The Fluid Kinetics-Poisson Module (FKPM) calculates the properties of neutral and charged species by solving their continuity, momentum, and energy equations and addresses the electrostatic potential by solving the Poisson equation. Electric fields are recorded as a function of position and phase during the RF cycle of the applied power. These fields, species densities, and fluxes are passed to the Electron Energy Transport Module (EETM). In the EETM, electron energy distributions (EEDs) as a function of position averaged over the RF cycle are calculated using Monte Carlo methods in the electron Monte Carlo Simulation (eMCS). EEDs are computed both in the bulk plasma and for electrons incident onto surfaces. The bulk plasma EEDs are used to compute electron impact source functions and transport coefficients that are used in the FKPM.

The eMCS separately produces EEDs for electrons originating in the plasma by volumetric processes (e.g., electron impact ionization, Penning ionization) and for electrons originating from surfaces (SEE, electric field emission, injected electron beams). The eMCS module initiates pseudoparticles in the volume or from surfaces and integrates their trajectories resulting from the spatially and phase-resolved electrostatic fields produced by the FKPM. Recording the electron trajectories then produces the EEDs that are used to generate source functions and transport coefficients for use in the FKPM.

The Plasma Chemistry Monte Carlo Module (PCMCM) computes EADs of ions and hot neutrals incident onto surfaces (the EADs of electrons onto surfaces are produced by the eMCS). The PCMCM launches pseudoparticles representing ions and neutrals and integrates their trajectories (including collisions) in the oscillating electrostatic fields using Monte Carlo techniques. The trajectories are tracked until the pseudoparticle strikes a surface when its energy and incident angle are recorded. The end result is three sets of EADs onto surfaces for ions, secondary electrons ($e_b$) that can produce beamlike distributions onto surfaces and bulk electrons.

A schematic of the CCP reactor used in this study is in Fig. 1. The reactor is cylindrically symmetric, consisting of two parallel electrodes with a radius of 15 cm separated by a 4.0 cm gap. A wafer is placed on the bottom electrode having a permittivity of $\varepsilon/\varepsilon_0 = 8$ and conductivity of $0.05\ \Omega^{-1}\ \mathrm{cm}^{-1}$. The grounded top electrode functions as a showerhead gas inlet. Sinusoidal RF power is applied to the bottom electrode. For cases when bias on the bottom electrode is nonsinusoidal (VWT), RF source power is also applied to the top electrode. The bottom electrode is surrounded by a dielectric focus ring with negligible conductivity, a relative permittivity of $\varepsilon/\varepsilon_0 = 4$, an outer radius of 17.6 cm, and an inner radius of 15 cm. The focus ring is surrounded by a pump port at the bottom of the computational domain.

When using sinusoidal bias waveforms, pure argon gas enters the reactor through the top inlet at a flow rate of 500 SCCM with pressure maintained at 10 mTorr at the entrance to the pump. A single frequency $f_0 = 20$ MHz bias is applied to the bottom electrode, with the voltage amplitude varied between $V_0 = 150$ and 450 V. The power supply is connected to the powered electrode through a 100 nF blocking capacitor, which gains a dc bias.

The consequences of using nonsinusoidal biases (VWT) on charging were investigated based on the ability of VWT to generate

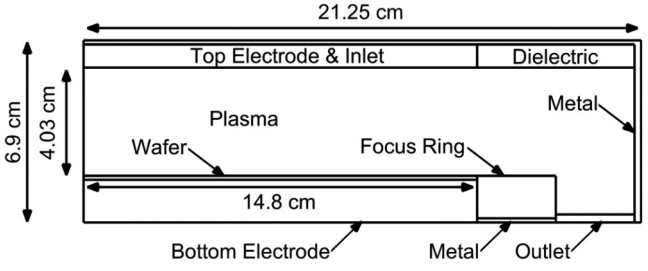


**FIG. 1.** Schematic of the reactor. In cases using a sinusoidal waveform, a 20 MHz bias is applied to the bottom electrode in pure Ar at 10 mTorr. In cases using a tailored waveform, a sinusoidal bias of 500 W at 40 MHz is applied to the top electrode. A 2000 W bias having a tailored waveform at 5 MHz is applied to the bottom electrode.

electron energy-angular distributions (EEADs) onto the wafer that have narrow angular distributions and higher energies than typically generated using sinusoidal biases. When investigating VWT, the same reactor geometry was used as in the sinusoidal waveform cases; however, an $Ar/O_2 = 80/20$ gas mixture was used (500 SCCM) while the outlet pressure was maintained at 40 mTorr. The oxygen additive and higher pressure produce more collisional transport for thermal electrons, which enhances electric field reversals that in turn produce the narrower and more energetic EEADs onto the wafer. However, the bulk ionization produced by VWT biases is sensitive to the details of the waveform. To stabilize the bulk plasma properties while changing the bias waveform, source power was applied to the top electrode using a sinusoidal frequency of $f_T = 40$ MHz with the amplitude being adjusted to deliver a constant power of $P_T = 500$ W. The VWT bias applied to the bottom electrode had a fundamental frequency of $f_0 = 5$ MHz, delivering a constant power of $P_0 = 2000$ W. The power supplies for both electrodes are connected through separate 100 nF blocking capacitors.

The nonsinusoidal voltage waveform used here and the resulting electric field reversal (EFR) are discussed in Ref. 8, and so only a brief description of VWT and its consequences are discussed here. The waveform employed here is composed of five fundamental sine waves,

$$V(t) = V_0 \sum_{k=1}^{5} \frac{4-k}{25+5k} \cos(2k\pi f_0 t + k\pi\varphi_k), \tag{1}$$

where $V_0$ is the total voltage amplitude, $k$ is the harmonic order, $f_0$ is the fundamental frequency, and $\varphi_k$ is the relative phase shift between different harmonics. For parametric studies, $\varphi_k$ was varied from 0° to 180° in 45° increments for $k = 2$ and 4. Varying $\varphi_k$ between different harmonics can alter the amplitude and length of the anodic period of the waveform. The system responds to short positive excursion of the applied potential by temporarily reversing the direction of the electric field from repelling electrons to attracting electrons toward the surface. By changing $\varphi_k$ different degrees of EFR can be produced, thereby offering a method to fine-tune the EEADs so that the effect of anisotropic electrons on SEE can be analyzed.

The reaction mechanism for the Ar and $Ar/O_2$ plasmas was adapted from a base $Ar/O_2/C_4F_8$ mechanism in Ref. 31, modified to exclude fluorocarbon species and include excited Ar states from Ref. 32. The ion-induced secondary electron yield (SEY) for metal and the wafer is 0.15, and dielectrics have an SEY of 0.05. The EADs and fluxes that are used as input to the MCFPM are averaged over the area of the wafer.

## III. DESCRIPTION OF THE FEATURE-SCALE MODEL

In both sinusoidal and VWT cases, EADs and fluxes collected wafer are used as input for the MCFPM for the simulation of charging of predefined features. The MCFPM is a 3D voxel-based model that simulates the etching and charging of features.[8,33,34] The algorithms used in the MCFPM have been discussed in detail on Ref. 33, and so are only briefly discussed here.

With a focus only on charging processes, the reaction mechanism used for the MCFPM does not change the shape or properties of the predefined feature (other than charging). The initial trajectory and energy of gas-phase pseudoparticles directed toward the wafer are randomly chosen from the EADs provided by the HPEM. The trajectories are integrated in time in the electric fields produced by charging of the feature. As this investigation is focused on charging of predefined features, only charged particles are directed toward the wafer. Ions are neutralized upon surface impact (becoming hot neutrals), and their charges are deposited at that incident location. Since we are investigating charging processes, the trajectory of the neutral particle is then not followed. There is negligible secondary electron emission by neutral particles having energies investigated here.

The electric potential within the feature, $\Phi$, is then calculated by solving Poisson's equation $-\nabla \cdot \varepsilon \nabla \Phi = \rho$, where $\varepsilon$ is the permittivity of the material and $\rho$ is the charge density. For the nonconducting dielectric materials used in the simulation, the charge density resides solely on the surface. Poisson's equation is solved using the method of successive-over-relaxation (SOR) using finite volumes for discretization. Reflective boundary conditions were used on the lateral sides of the computational domain. The top and bottom of the domain were held at zero potential.

The algorithms employed in the MCFPM for SEE were improved to address the energy and angle dependent emission of SEs by ion- and electron impact. When ions and electrons collide with surface materials, MCFPM calculates the yield of SEs based on the material type, energy, and angle of the incident particle. The number of electrons that are released from the surface is statistically determined in the event of electron impact. If more than one electron is emitted, the first SE can originate from backscattering based on a material-dependent backscattering probability. In the event of ion-impact, only true secondary electrons (TSEs) are emitted. A backscattered SE is, conceptually, the same electron as was incident. A true secondary electron originates from within the material. It is not possible to physically distinguish a backscattered electron from a true secondary. This distinction is typically made based on the energy and angular distribution of the emitted SE.

The energy dependence of ion-induced SEE typically contains an initial region of relatively constant SEY, as shown in Fig. 2.[35,36] This region of constant SEY is attributed to Auger neutralization or potential ejection. The approaching ion brings with it an electric potential, which produces an intense electric field when approaching within a few angstroms of the surface. This large electric field produces band-bending in the solid, which enables electrons to tunnel through the potential barrier that confines them to the solid. The first electron that leaves the surface neutralizes the incident ion and is not typically counted as an SE. Statistically, a second electron may escape the solid before the potential barrier is restored upon neutralization of the ion. The additional escaping electron is classified as an SE. The SEY is relatively constant and dominated by Auger neutralization up to about a keV of ion energy. The SEY yield of Auger neutralization typically does not depend on the angle of incidence of the ion. The SE is emitted with an isotropic Lambertian angular distribution and an average energy of a few eV depending on the identity of the materials [a Lambertian distribution scales as $\cos(\theta)$, where $\theta$ is measured relative to the normal to the surface].

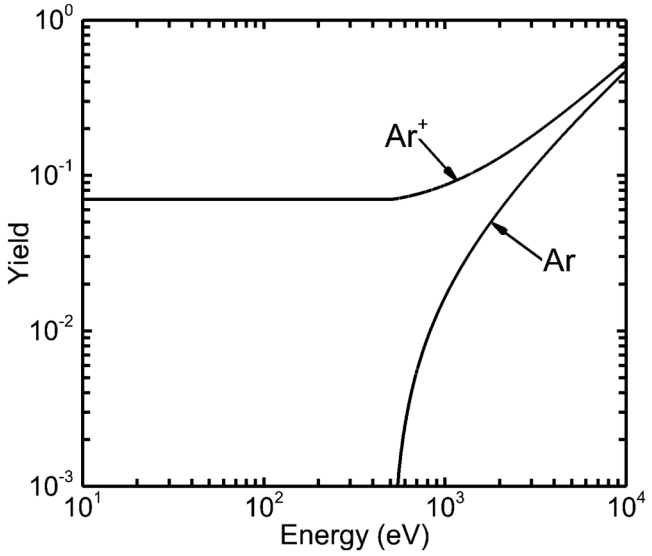


**FIG. 2.** Secondary electron emission yield of clean metal surfaces by argon ion and neutral argon impact as a function of energy. (Ref. 35) Adapted from Phelps and Petrovic, Plasma Sources Sci. Technol. **8**, R21 (1999). Copyright (1999) IOP Publishing.

At energies higher than those dominated by Auger neutralization, the SEY increases with increasing ion energy, a process described as kinetic ejection (KE).[35,37–39] KE refers to the direct kinetic energy transfer from ions to electrons through knock-on collisions between the ions and electrons residing in the material. This mechanism is conceptually identical to the physical mechanism for electron-induced SEE.[37,39,40] In the KE regime, the SEY yield scales as $\cos^{-1}(\theta)$, increasing toward grazing, for $\theta < 60°–80°$.[37,38,40,41] However, the experimental and analytical relationships of SEY for $\theta > 60°–80°$ are still unclear.[25,39] If KE is solely due to the elastic exchange of energy between energetic incident particles and electrons residing in orbitals or bands, then analogies could possibly be made between KE and physical sputtering. The yield would then have an initial increase as θ increases from the normal reaching a maximum (typically near 60°) before decreasing to essentially zero at a grazing angle of 90°.[42]

The angular dependence of KE does not significantly affect the yield for the ion energies of interest in this paper, which are below 2 keV.[43] The yield is then simplified to have an initially constant value at low energies and a linearly increasing dependence on energy beyond a threshold energy with angular dependency omitted,

$$\gamma_i(E) = \gamma_0, \quad E \le E_t,$$
$$\gamma_i(E) = \gamma_0 + \frac{d\gamma_i}{dE} \cdot (E - E_t), \quad E > E_t, \tag{2}$$

where $\gamma_0$ is the initially constant yield constant and $\frac{d\gamma_i}{dE} \cdot (E - E_t)$ addresses the additional yield above the threshold energy $E_t$ in kinetic ejection regime. When emitting ion-induced SEs, the outward trajectory is randomly chosen from a Lambertian angular distribution cos(θ), which favors emission in the direction of surface normal. While energetic hot neutrals are capable of inducing secondary emission (Fig. 2), the threshold energy is high enough that most of the neutral particles in the systems of interest do not have sufficient energy to induce SEE. In the event that the neutral particles are above threshold, the yield is typically small and so neutral-induced SEE was neglected here.

When electrons strike a surface, two types of SEs can be emitted: backscattered and true SEs. Backscattered SEs (BSEs) correspond to the primary electron that is nearly elastically scattered with a probability $\eta$. Due to the inefficient elastic energy exchange between heavy atoms in the material and electrons, the energy of the primary electron is largely preserved[27,44,45] upon backscattering. The backscattering probability, $\eta$, is given by

$$\eta(E, \theta) = \eta_0(E) \exp[\eta_1(1 - \cos\theta)], \tag{3}$$

where $E$ is the energy of the incident electron in keV, $\theta$ is the angle of incidence with respect to the surface normal, and $\eta_0(E)$ is the backscattering probability at normal incidence,

$$\eta_0(E) = \{[\log(E/0.05)\Theta(E-0.05)\Theta(1.0-E)/\log(20)] + \Theta(E-1.0)\} \times \left[0.1\exp(-E/5) + 1 - (2/e)^{0.037Z}\right], \tag{4}$$

where $\eta_1 = -\log[\eta(E,0)]$, Θ is the Heaviside step function for capturing different energy ranges, and $Z$ is the atomic number of the surface species with which the electron collides.[46] When emitted, the angular distribution of BSEs is Lambertian for normal incidence and becomes increasingly specular as the incidence angle approaches grazing.[21] When an electron strikes a surface, the corresponding yield is computed and a random choice is made based on their respect yields, whether to backscatter the primary electron or not.

The MCFPM treats backscattering events and true emission as two independent processes. The primary electron can be backscattered regardless of whether TSEs are emitted or not and vice versa. For a backscattering event, the primary electron is specularly reflected with an additional thermal velocity component to represent its interaction with the surface. If a TSE is emitted during the same collision with the surface, the energy of the TSE is subtracted from the energy of the BSEs for energy conservation. The underlying assumption is that energy is not extracted from the material surface. The TSEs typically follow Lambertian angular distributions and depending on the material the shape may become narrower or broader.[24,47] For this study, a perfect Lambertian distribution for emitted TSEs was used.

TSEs are defined as electrons that escape from the orbitals of the material due to inelastic collisions between the primary electron and the material and typically leave the material with an energy under 50 eV. The energy of most TSEs is under 5 eV.[20,26,44,48] When electrons strike a surface, the secondary-emission yield is calculated and the number of SEs that should be emitted is

statistically determined. The TSE yield $\delta$ is given by

$$\delta(E,\theta) = c_1\left[R_u\left(\frac{dR}{dE}\right)^{-1}\frac{1-\exp(-Q)}{Q} + R_u^2\frac{d^2R}{dE^2}\left(\frac{dR}{dE}\right)^{-3}\frac{1-(Q+1)\exp(-Q)}{Q^2}\right], \quad (5)$$

where $R = r_1E^{n_1} + r_2E^{n_2}$, $Q = c_2R\cos\theta$, and $E$ and $\theta$ are the energy and angle of the incident electron, respectively.[45] $R_u$ is the lesser of the solutions of $\frac{dE}{dx}\big|_{R_u} = 0$ and $\int_0^{R_u}\left|\frac{dE}{dx}\right|dx = E$, where

$$\frac{dE}{dx} = \left(\frac{dR}{dE}\right)^{-1} + \frac{d^2R}{dE^2}\left(\frac{dR}{dE}\right)^{-3}x, \quad (6)$$

where $c_1$, $c_2$, $r_1$, $r_2$, $n_1$, and $n_2$ are parameters and were obtained from Ref. 45. In general, the following general assignments are initially made: TSE yields for $SiO_2$ were assigned to all dielectric materials, aluminum yields were assigned to all metals, and yields for Teflon are assigned to all polymers. If data are available for a specific material, these assignments are replaced. In this investigation, the only material exposed to plasma is photoresist (PR) and $SiO_2$.

The yield of electron-induced SEE rises from zero at zero energy to a maximum yield of more than 1.0 at around a 300–600 eV incident energy and then slowly decreases with increasing incident energy.[27,44,45] When the total SEY is larger than one, electron impact events on average induce positive charging at the location of incidence. Otherwise, there is on the average negative charging.

In this paper, we discuss the steady-state charging of predefined structures to provide insights into how SEE influences charging outcomes while keeping the feature's structural dimensions unchanged. The aim of this paper is to capture a steady-state *snapshot* of the electric potential profile across different aspect ratios under varying plasma conditions. Allowing the feature to evolve during charging, as in actual etching, would complicate interpretation of the contributions of different secondary-emission processes. That said, the steady-state potential is reached on a much shorter time scale than that of feature evolution.[5,18] As a result, the potentials discussed here can be considered a quasisteady state approximation of the potential that occurs in an evolving feature when it reaches a specific configuration.

The predefined features used in this investigation are shown in Fig. 3. The first set of features are finite-depth trenches [Fig. 3(a)]. Although the feature is nominally two-dimensional, the simulations are performed in three-dimensions with there being a finite depth. The finite depth enables a naturally occurring statistical variation in properties in the direction of the depth that produces more realistic outcomes. The trench geometry consists of a 375 nm thick silicon stop layer, a 4625 nm thick $SiO_2$ layer, and a 1250 nm thick PR layer. The feature is pre-etched to a depth of 5000 nm (including the mask) with widths of 300, 200, and 100 nm to produce ARs of 16.7, 25, and 50, respectively. The sidewall thickness on each side was kept at 200 nm for all ARs. The finite depth is 50 nm. The mesh is 140, 120, and 100 voxels wide for the increasing ARs, 1250 cells tall and 10 cells deep, resulting in cubic voxels 5 nm on a side. Via features, shown in Fig. 3(b), were also investigated. The via feature consists of a 150 nm thick Si stop layer, a 1850 nm thick $SiO_2$ layer, and a 150 nm thick PR layer. The pre-etched hole has a depth of 2000 nm, a diameter of 100 nm, and an AR of 20 (including the mask). The top edge of the via is chamfered with a 25 nm width and 30 nm depth. The mesh is 60 cells wide, 60 cells deep, and 460 cells tall producing cubic voxels that are 5 nm on a side. The simulations are run until a steady-state potential distribution is achieved.

The base case has a constant ion-induced SEY of 0.1 for $SiO_2$ and 0.05 for the PR. While electron-induced SEY data are available for $SiO_2$, the yield data for PR are lacking. For this study, the electron-induced SEY of PR was assigned a constant value of 0.10. The PR and $SiO_2$ have different permittivities ($\varepsilon/\varepsilon_0 = 3$ and 4).

## IV. REACTOR-SCALE PLASMA PROPERTIES

### A. Sinusoidal waveform

The charging processes in a single sinusoidal frequency 20 MHz CCP sustained in 10 mTorr of pure argon were investigated for voltage amplitudes of 150, 300, and 450 V. The plasma properties of the base case having amplitude $V_0 = 300$ V are shown in Fig. 4. The plasma density peaks essentially at midgap and on axis at $5.2 \times 10^{10}$ cm$^{-3}$ with a reactor average of $3.2 \times 10^{10}$ cm$^{-3}$. On a time average basis, the bulk plasma potential is 65 V, with a dc bias of −168 V, resulting in a time average potential drop of 233 V across the sheath. The sheath is uniform with some curvature at the transition between the wafer and the focus ring. Power deposition is 261 W, while 14.8 W (5.7% of the total) is deposited into electrons. The peak electron temperature near sheath edges is 3.7 eV with an average of 2.7 eV.

With voltage amplitudes from 150 to 450 V, profiles of plasma properties are essentially the same. The power deposition and maximum (and average) plasma density varies from 77 W and $2 \times 10^{10}$ cm$^{-3}$ (average $1.3 \times 10^{10}$ cm$^{-3}$) for $V_0 = 150$ V to $7.2 \times 10^{10}$ cm$^{-3}$ (average $3.2 \times 10^{10}$ cm$^{-3}$) for $V_0 = 450$ V. The dc bias is −74 V for $V_0 = 150$ and −272 V for $V_0 = 450$ V, corresponding to sheath potentials of 120 and 350 V.

The wafer-average EADs of $Ar^+$ and $e_b$ are shown in Fig. 5. All EADs of bulk electrons are thermally distributed and so only the $V_0 = 300$ V case is shown. The characteristic bimodal energy distribution of $Ar^+$ represents the nearly collisionless transport of ions through the sheath, with a low-energy tail representing the ions that experience a collision, arriving with little no tilt from the normal. With increasing voltage amplitude, the maximum energy increases and angular spread decreases. At $V_0 = 150$ V, $Ar^+$ has an average angular breadth of ±2.0° and an average energy of 102 eV. At $V_0 = 300$ V, the angular breadth is ±1.5°and the average energy is 211 eV. At $V_0 = 450$ V, the angular breadth is ±1.3°, and the average energy increases to 324 eV. As ion energies are less than 1000 eV, the ion-induced SEE does not enter the kinetic ejection regime. As a result, the ion-induced SEY has no energy dependency and will have a constant yield of 0.10 for $SiO_2$.

While the EADs of ions do not have angular asymmetries, the EADs of $e_b$ do have an angular skew with a positive incidence angle at higher energies (trajectories pointing inward toward the center of the wafer) and negative incidence angle at lower energies

(trajectories pointing outward). During one RF cycle, the charging and discharging of the focus ring create time-varying electric fields in the horizontal direction. The electric fields pointing outward during the anodic period accelerate high-energy $e_b$ inward, resulting in a positive incidence angle. The electric fields point inward during the cathodic period accelerating low-energy $e_b$ outward resulting in a negative angle. The distortion increases approaching the wafer edge being closer to the focus ring. However, the overall degree of distortion is small, as the average angle of deflection is at most 0.2°. The light electrons respond quickly to these time-varying electric fields, which enable this skew to the EEAD. Ions, being heavier, with a longer transit time, average the oscillating horizontal component of the electric field.

The fluxes of charged species at midwafer ($r = 7.5$ cm) are shown in Fig. 6. Fluxes increase with voltage amplitude though at a slower rate than the increase in power as the majority of the incremental power goes into ion acceleration. The fluxes of $Ar^+$ and bulk electrons are essentially the same, with the disparity being made up by the flux of $e_b$, which is an order of magnitude lower.

### B. Voltage waveform tailoring

In the quasisteady state in RF excited CCPs, the cycle averaged fluences of electrons (and negative ions) and positive ions to the substrate must be equal. For voltage waveforms having short positive going excursions, electron diffusion across the sheath may not provide sufficient fluence to balance the positive ion fluence. For these conditions, an EFR is produced in the presheath and sheath in order to accelerate electrons into the substrate to balance the ion fluence. VWT producing nonsinusoidal waveforms with short positive excursions can produce such EFRs, resulting in electron energies onto the wafer of many tens to hundreds of eV with a narrow angular spread. One of the original motivations for VWT technologies was to produce energetic and narrow angle electron fluxes into the wafer to reduce in-feature positive charging.

To investigate the role of electrons for inducing SEE and consequences on charging, a dual-frequency CCP system sustained in an $Ar/O_2 = 80/20$ gas mixture at 40 mTorr having a VWT bias was used. A 40 MHz bias of 500 W with a sinusoidal waveform was applied to the top electrode, and 2000 W VWT bias was applied to the bottom electrode at a fundamental frequency of 5 MHz. The

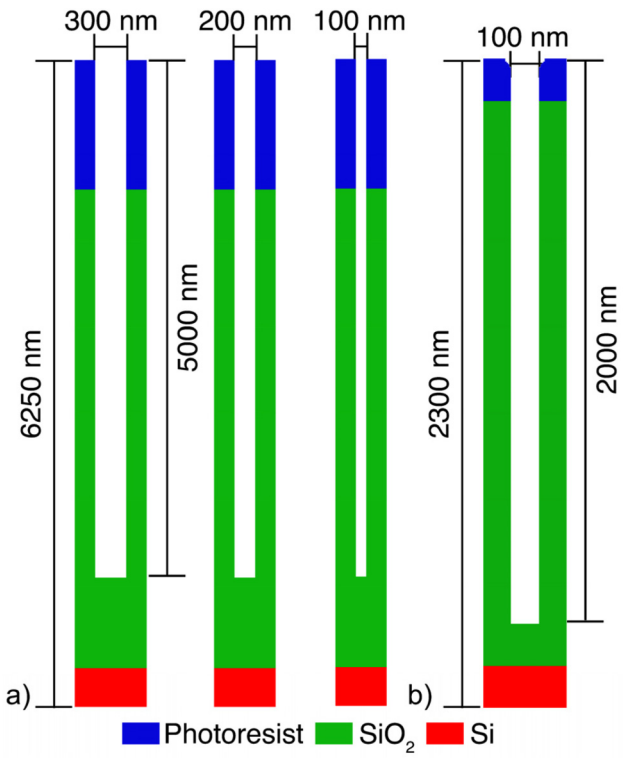


**FIG. 3.** Schematics of the predefined trench features having aspect ratios of (a) (left to right) 16.7, 25, 50 and (b) for a via having AR = 20.

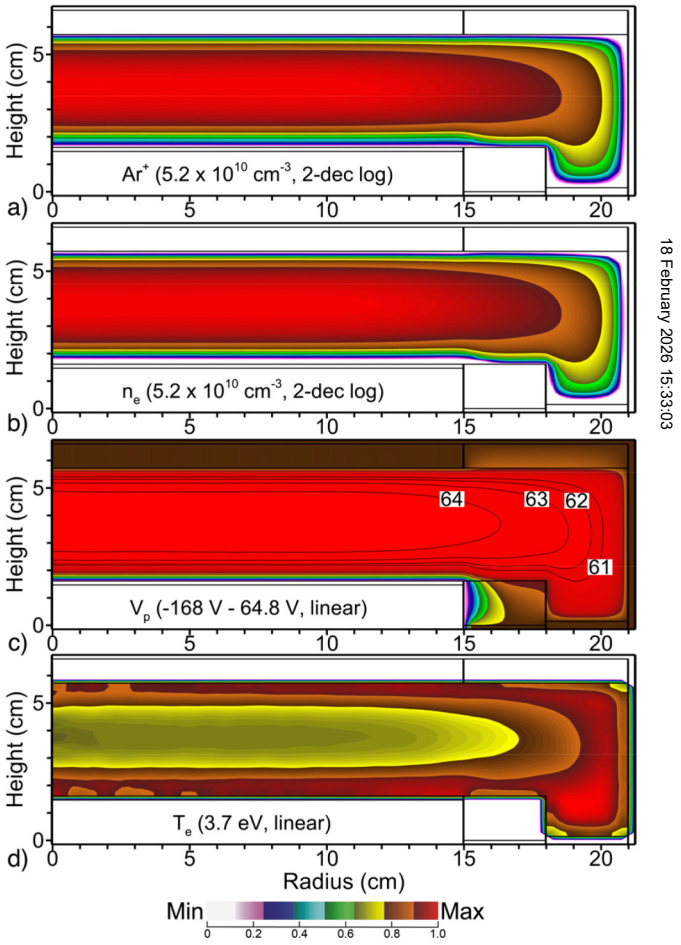


**FIG. 4.** Reactor-scale properties of the Ar CCP base case with $V_0 = 300$ V, $f_0 = 20$ MHz, $P = 10$ mTorr. Time averaged (a) $Ar^+$ density, (b) electron density, (c) plasma potential, and (d) electron temperature.

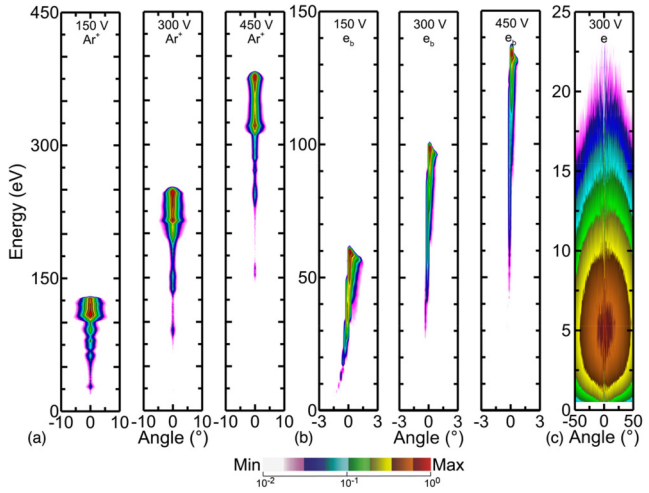


**FIG. 5.** Wafer-averaged energy and angular distributions of (a) argon ions and (b) $e_b$, beamlike secondary electrons. (c) EADs for bulk electrons for $V_0 = 300$ V (2-decade log scale).

gas composition was chosen to increase the magnitude of the EFR by making the plasma more resistive compared to pure Ar, and so tune the initial energy of incident electrons so that different degrees of SEE can be induced. The phase shift of the second and fourth harmonics was varied between $\varphi_{2,4} = 0°$, 45°, 90°, 135°, and 180° with $\varphi_{2,4} = 0°$ being the base case.

Reactor-scale plasma properties for the base case are shown in Fig. 7. The steady-state voltage amplitude on the top electrode is

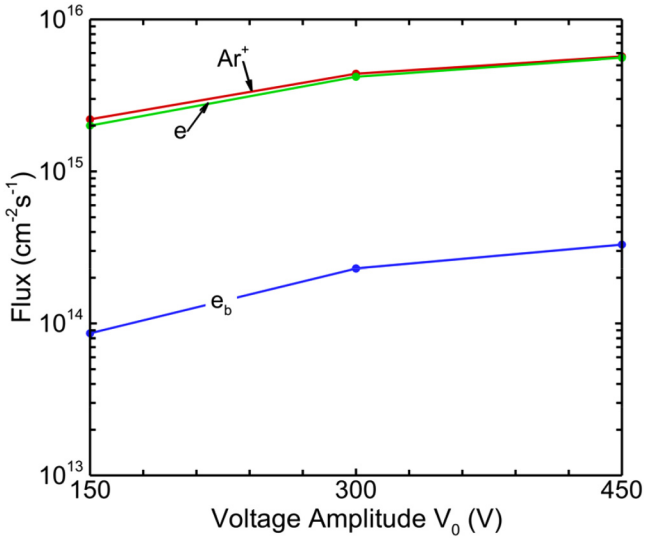


**FIG. 6.** Fluxes of charged species onto the wafer at r = 7.5 cm as a function of voltage amplitude with a sinusoidal waveform.

$V_T = 277$ V and that on the bottom electrode is $V_0 = 1841$ V with a dc bias of −1133 V. Plasma densities are a few times $10^{11}$ cm$^{-3}$, dominated by $Ar^+$ with the negative ion density of $O^-$ being about 30% that of the positive ion density. During the peak of the anodic period, an electric field reversal occurs in the sheath above the wafer. Electric field vectors point away from the wafer, accelerating electrons into the wafer. The duration of the EFR is 15 ns, which is 7.5% of the RF cycle.

The applied voltage waveforms on the bottom electrode over one RF cycle for $\varphi_{2,4} = 0°$, 45°, 90°, 135°, and 180° are shown in Fig. 8(a). The densities of ions and electrons, and their spatial distribution in the reactor remain, and their fluxes to the wafer are similar for all values of the phase offset, as shown in Fig. 8(b). In the dual-frequency CCP, the high frequency power largely determines the magnitude of the ion fluxes whereas the low frequency power largely determines the ion (or electron) acceleration into the wafer. With the HF power being constant, the fluxes to the wafer are largely constant.

The charged particle energies and sustaining voltages are sensitive functions of phase offset. The voltage amplitude of the top electrode $V_T$, the voltage amplitude of the bottom electrode $V_0$, and the magnitude of DC self-bias on the bottom electrode $V_{DC}$ are shown in Fig. 8(c) as a function of phase $\varphi_{2,4}$. As $\varphi_{2,4}$ changes from 0° to 180°, $V_T$ remains essentially constant at around 250 V as the substrate bias produces little electron heating and so the power delivered by $V_T$ is well decoupled from the substance bias. $V_0$ increases from 1841 to 4280 V for $\varphi_{2,4} = 0°$–180° to draw more ion current toward the surface during the shorter cathodic period to achieve the same power deposition. The magnitude of the DC self-bias decreases from $V_{DC} = -1133$ V at $\varphi_{2,4} = 0°$ to $V_{DC} = -489$ V at $\varphi_{2,4} = 180°$ to balance electron and ion currents to the substrate. As the phase shift increases, with a larger fraction of the period being positive voltage, balancing currents requires a smaller magnitude of the dc bias.

The fluxes of $e_b$ are most sensitive to phase shift. The sources of the beam electrons are either secondary emission from the top electrode that crosses the gap and the sheath at the bottom electrode, or are emitted from the bottom electrode and reflect from the sheath at the top electrode. At a large phase angle, the sheath is mostly anodic, which enables electrons emitted from the top electrode to reach the bottom electrode, and so the $e_b$ flux increases. While electric field reversal draws electrons toward the wafer, $O^-$ does not have a significant flux onto the surface because of its large inertia compared to electrons.

The mean energies of the charged species striking the wafer are plotted in Fig. 8(d). The corresponding energy and angular distributions for ions (IEAD), electrons (EEAD), and $e_b$ (EBEAD) are shown in Fig. 9. At all phase shifts, the IEADs exhibit a multimodal profile with larger portion of ions shifting toward the lower energy peak as $\varphi_{2,4}$ increases from 0° to 180°. This shift is a consequence of a larger fraction of the RF cycle being the anodic phase compared to the ion-accelerating cathodic phase. The maximum in the IEAD at 2000 eV for $\varphi_{2,4} = 180°$ corresponds to the lightest ion, $O^+$, that is better able to respond to the short cathodic phase.

The electron fluxes, accelerated by EFR at low phase shift, reach energies approaching 140 eV with an angular spread of <20°, compared to nearly isotropic fluxes with energies of a few eV in the

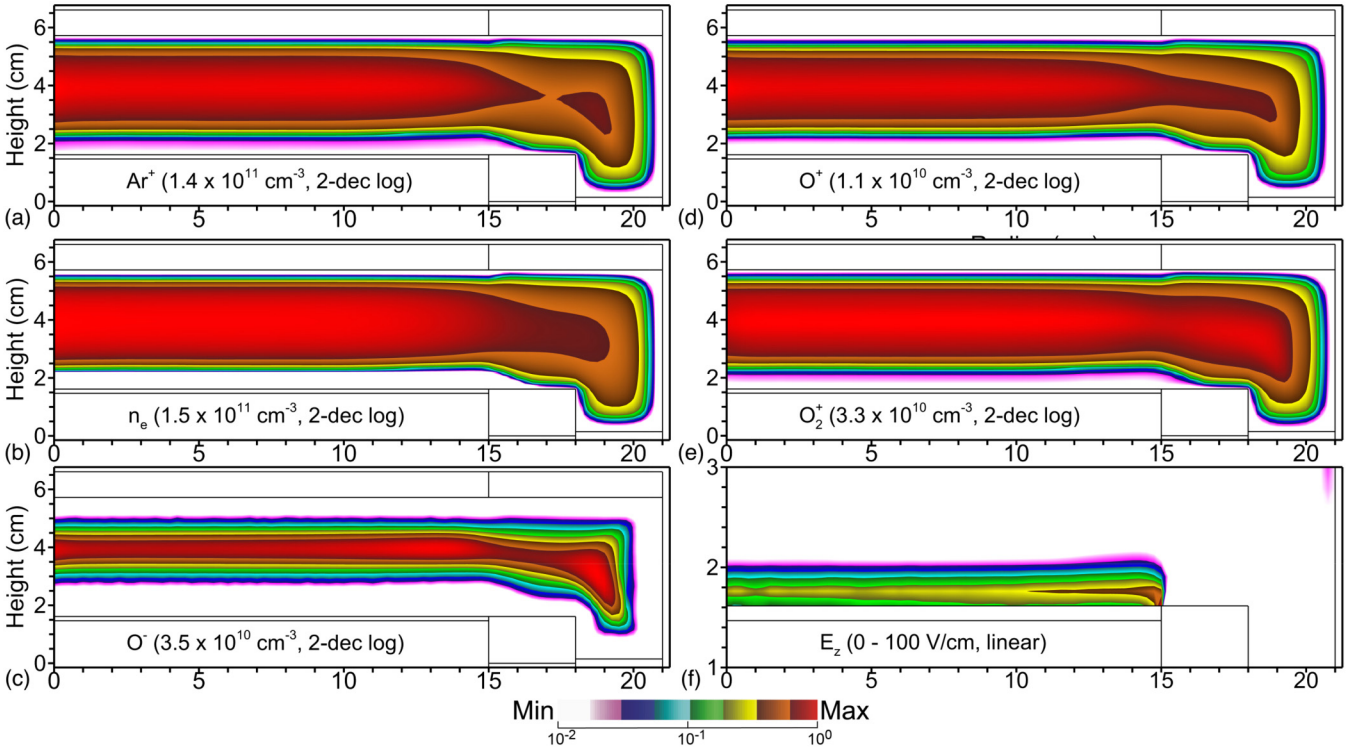


**FIG. 7.** Reactor-scale properties for the $Ar/O_2 = 80/20$ (40 mTorr) dual-frequency CCP base case with a bias power of 2000 W at 5 MHz using VWT with $\varphi_{2,4} = 0°$ and high frequency power of 500 W at 40 MHz. Time averaged densities of (a) $Ar^+$, (b) electrons, (c) $O^-$, (d) $O^+$, and (e) $O_2^+$. (f) Reversed axial electric field near the wafer during the anodic period. Densities that are plotted on a 2-decade log scale have the maximum noted in each image.

absence of EFR. With increasing phase angles, the EEADs decrease in energy with the average energy decreasing from 74 eV at $\varphi_{2,4} = 0°$ to 26 eV at $\varphi_{2,4} = 180°$ due to the weaker EFR. The mean energy of the flux of $e_b$ first decreases from 397 eV at $\varphi_{2,4} = 0°$ to 93 eV as $\varphi_{2,4}$ increases to 90° and then increases to 272 eV at $\varphi_{2,4} = 180°$. $e_b$ are energetic enough to have an SEY of more than unity, and the majority of $e_b$ strike the wafer nearly perpendicularly. However, the fluxes of $e_b$ are at most 4%–5% of the fluxes of positive ions when $\varphi_{2,4}$ is below 180°. As a result, their contribution to the overall charging and SEE may not be significant. The promotion of beam electrons to higher energies at the large values of phase shift reflects their better ability to cross the anodic sheath.

## V. CHARGING OF PREFORMED DIELECTRIC FEATURES

The general behavior of SEE during the charging process across different structures and EADs is first examined by analyzing the charging of trench and via features when using a sinusoidal bias waveform. The role of ions in this process was assessed by varying the ion-induced SEY. The role of anisotropic electrons in charging was investigated by comparing trench charging using fluxes and EADs from a tailored waveform system with results obtained using the same fluxes and IEADs while using a low-energy thermal electron EEAD.

### A. Charge redistribution

The steady-state electric potentials are shown in Fig. 10 for predefined trench features with aspect ratios of 16.7, 25, and 50, with and without. SEE. The plasma conditions are the sinusoidally excited CCP (10 mTorr, Ar, 20 MHz) with voltage amplitudes of at 150, 300, and 450 V. For $V_0 = 150$ V, in the absence of SEE, the potential is maximum at the bottom of the trench for ARs of 16.7 and 25. With the smaller aspect ratios, the majority of positive ions can reach the bottom of the trench prior to striking sidewalls in neutralizing collisions. The maximum potentials are 108 and 112 V for ARs of 16.7 and 25, respectively. When the width is sufficiently narrow, as with an AR of 50, ions first strike and neutralize on the sidewalls before reaching the bottom of the feature, producing a maximum in plasma potential of 112 V at height that corresponds to an AR of approximately 25. The maximum positive potential for all AR is lower than the maximum ion energy of 125 eV. In the steady state, the negative and positive charged particle fluxes to the dielectric surfaces must be equal at all locations. While the flux balance at the top is more easily achieved, the balance at the trench bottom is accomplished by the positive potential in the feature accelerating thermal electrons into the feature to neutralize positive charge. The incident electrons have energies of only a few eV and are accelerated into

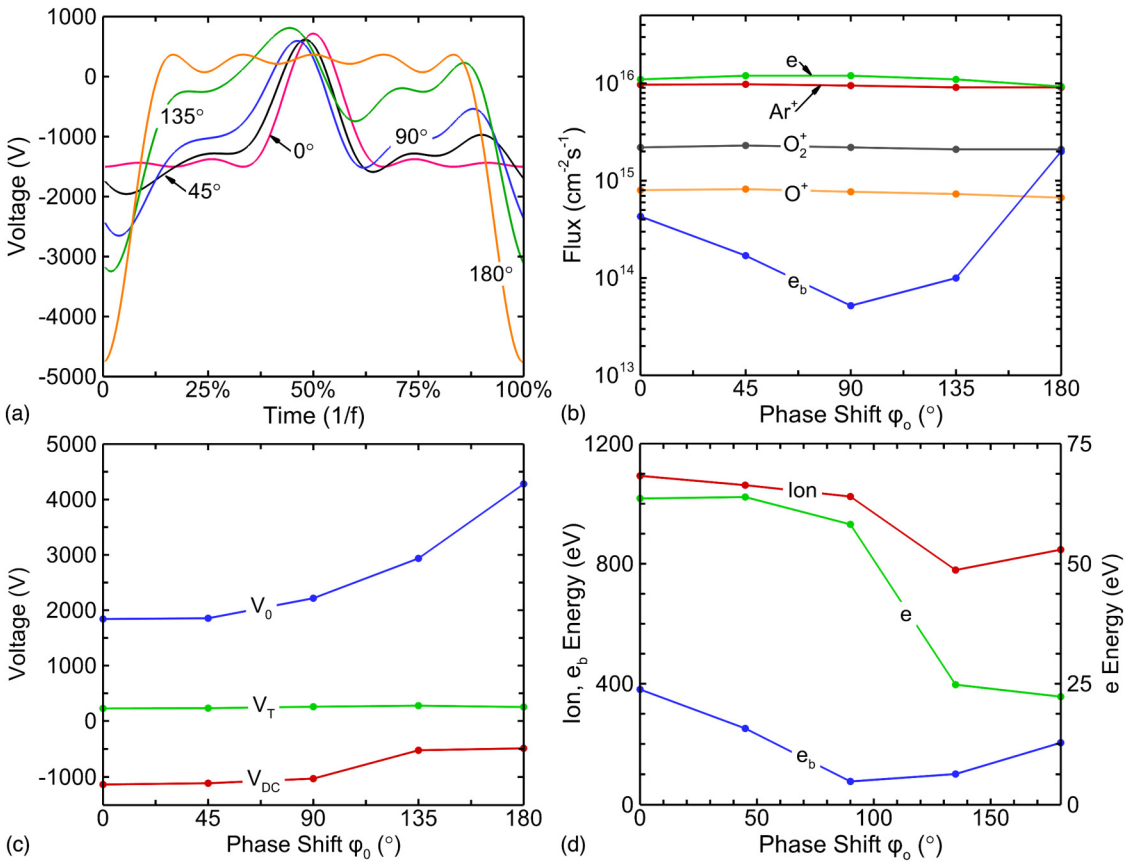


**FIG. 8.** Plasma properties for the dual-frequency $Ar/O_2$ CCP with a VWT bias on the lower electrode while maintaining 2000 W bias power. (a) Voltage on the bottom electrode during one RF cycle for $\varphi_{2,4} = 0°$, 45°, 90°, 135°, and 180°. (b) Fluxes of charged species onto the wafer at r = 7.5 cm, (c) voltage amplitude of the bias on the top electrode $V_T$, bottom electrode $V_0$, and the magnitude of DC self-bias on the bottom electrode $V_{DC}$, and (d) average ion, electron, and $e_b$ incident energy collected at the wafer as a function of phase shift $\varphi_{2,4}$.

the feature to energies greater than that of the positive potential. The electron arrives with its initial energy plus the energy due to acceleration by the positive potential. (For our conditions, there are no gas-phase electron collisions in or directly above the feature.) The negative charge from the accelerated electrons compensates for the positive ions arriving with energies greater than the local positive potential.

With $V_0$ increasing from 150 to 300 V (maximum ion energy of 250 eV), the maximum potential inside the feature increases to 211, 225, and 227 V for ARs of 16.7, 25, and 50, respectively. For $V_0 = 450$ V (maximum ion energy 380 eV), the maximum potential for ARs of 16.7, 25, and 50 increases to 315, 330, and 344 V, respectively. The maximum potential for the smaller AR remains at the bottom of the feature. The location of the maximum potential for an AR of 50 shifts downward in the feature with increasing $V_0$. These results at large ARs agree with past findings.[5,17,18]

When including SEE, there is a reduction in electric potential. The degree of reduction increases with increasing voltage amplitude and decreasing aspect ratio. With $V_0 = 150$ V, there is no significant change in the global maximum in potential when including SEE whereas the maximum potential shifts to being lower in the feature. With $V_0 = 300$ V, there is a 5% reduction in the global maximum in potential for AR = 16.7 and 3% for AR = 25 with a downward shift of the maximum potential. The maximum potential for AR = 50 decreases by 1%. With $V_0 = 450$ V, there is a significant redistribution of charge in the feature. The reduction in maximum potential is 16%, 13%, and 2% for ARs of 16.7, 25, and 50, respectively.

The reduction in potential within the feature is due to the redistribution of charge resulting from SEE. In the absence of SEE (and with nonconducting dielectric material), there is no mechanism to transfer charge within the feature after charge has been deposited at the initial location of incidence (assuming no spontaneous or electric field induced desorption of negative surface charge). The most energetic ions having a narrow angular spread can reach and charge the deeper parts of the trench, while the least energetic ions with broader angular spread typically strike the sidewalls of HAR features. Electrons, which initially have low energies and broad angles, are accelerated toward the maximum potential in

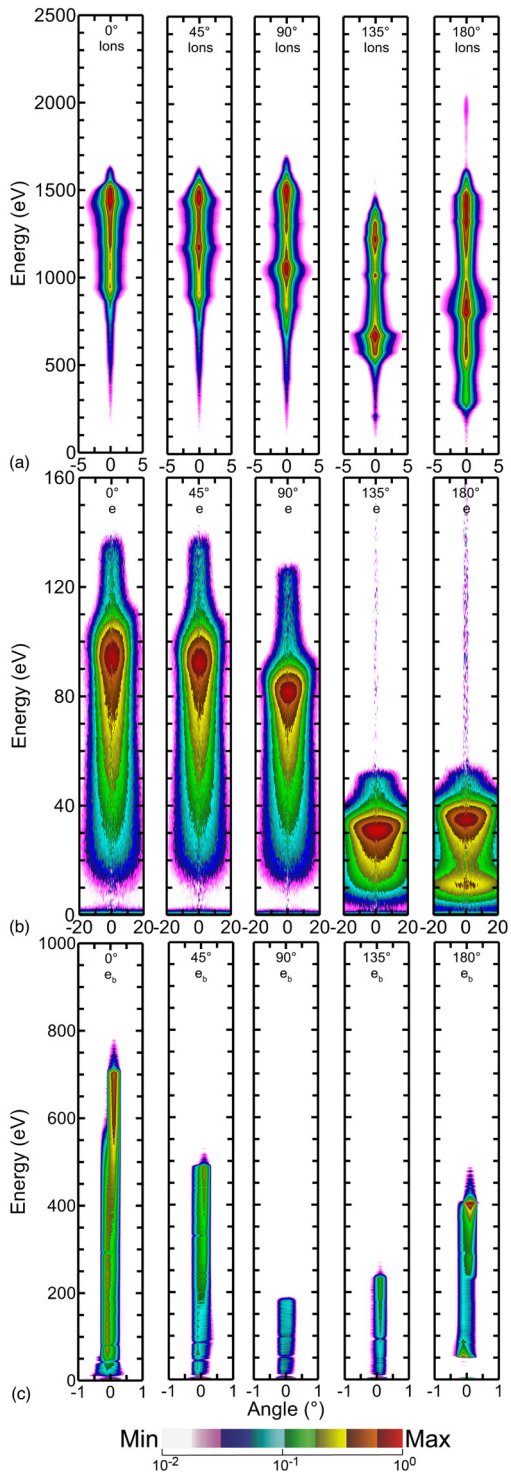


**FIG. 9.** Wafer-averaged energy and angular distribution of (a) all ions ($Ar^+$, $O_2^+$, $O^+$), (b) electrons and (c) $e_b$ for $\varphi_{2,4} = 0°$, 45°, 90°, 135°, and 180° (two-decade log scale).

the feature, balancing the incident positive charge everywhere in the trench at steady-state. With a low conductivity material, the charges remain essentially at the original site of incidence. Charge can be neutralized in place but does not move. It is true that the trajectories of incident charges are affected by the electric fields produced by previously deposited charge, as exemplified by the acceleration of thermal electrons into the feature. However, the steady-state charge distribution in the absence of SEE depends solely on the EADs of charged particles and the geometry of the feature.

When including SEE, secondary electrons emitted from the site of incidence of the ion or electron can propagate further into (or out of) the feature. The resulting potential distribution is then not strictly determined by the EADs of the incident particles. When SEs are emitted from less positive locations, they are accelerated toward the more positive locations to neutralize positive charge. When SEs are emitted from locations of maximum potential (e.g., at the bottom of the AR = 25 feature with $V_o = 300$ V), the electrons are trapped in the potential well and have limited ability to transport elsewhere. SEs are initially emitted with a Lambertian angular distribution with energies of up to 50 eV although most have energies of less than 5 eV. These trajectories of the more energetic SE could lead to some moderate redistribution of charge even if the electron is emitted from the maximum in plasma potential.

Inherently, charge redistribution is a transport process and depends on the total yield of emitted SEs. In the absence of electric field reversals, the electrons in the incident flux onto the feature are typically not energetic enough to initially produce significant SEE. However, these electrons are accelerated into the feature by previously deposited positive charge to gain energies at least equal to the positive potential at their site of incidence. These energies can be large enough to produce significant SEs. This maximum potential in the feature increases with increasing $V_o$. The average SEY (number of emitted SEs per incident charged particle) increases with voltage amplitude at all three ARs, as shown in Fig. 11. As a result, increasing voltage amplitudes indirectly raises the overall SEY of electrons, which, in turn, redistributes charge producing a reduction in potential compared to the absence of SEE.

The degree of charge redistribution is limited by the AR of the feature (spatial confinement). As shown in Fig. 10, when the AR increases, the change in electric potential with SEE decreases. A larger width (which for constant depth is a smaller AR) allows emitted SEs to transport further from their site of generation. A smaller width (larger AR) restricts SE to deposit their charge at nearby locations. Depending on the AR and voltage, the potential within the feature can vary by as much as 50% with SEE compared to without SEE.

The consequences of charge redistribution are shown by the electric potentials along the sidewall of the features appearing in Fig. 12. These potentials are shown when including and excluding SEE for voltages of 150–450 V. The discontinuity at 1.25 $\mu$m from the top of the feature corresponds to the interface between the PR and $SiO_2$. The general trend is that including SEE produces larger potentials near the top of the feature and lower potentials near the bottom of the feature with the effect being greater at lower AR. With lower AR (less spatial confinement), SEE initiates transport of electrons from the top of the feature toward the bottom of the

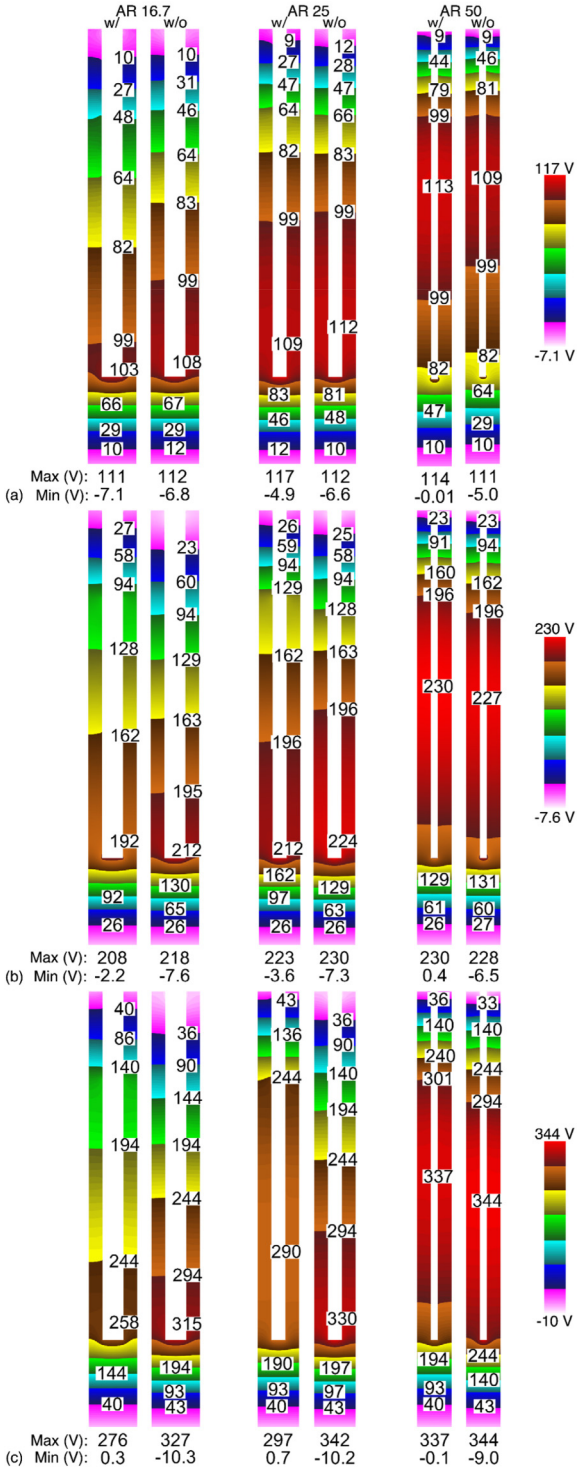


**FIG. 10.** Electric potential of trenches with (labeled "w/") and without (labeled "w/o") SEE at ARs of 16.7 (pair on the left), 25 (pair in the middle), and 50 (pair on the right) for voltage amplitudes of (a) 150, (b) 300, and (c) 450 V.

feature, leaving the top of the feature more positive, while neutralizing positive charge at the bottom of the feature leaving those locations less positive.

The flux and energy of electrons incident onto the surfaces of a feature with AR = 25 and $V_o = 300$ V are shown in Fig. 13. For these conditions, the electron fluxes incident onto the surface have low initial energies (around 5 eV) and broad angular distributions, as shown in Fig. 5. The positive potential that is produced in the feature due to the ions arriving with higher energies accelerates electrons into the feature. Given the low gas pressure and small feature size, there are essentially no gas-phase collisions in the feature. As a result, the electrons arrive at the surface with the sum of their initial energy (typically small) and the local electrical potential. In the absence of SEE, there is no additional electron transport beyond the initial collection on surfaces. The end result is that the electron energies striking surfaces closely match the potential profile within the feature. For these conditions, electrons strike the surface with energies up to 238 eV. The steady-state potential profile is an outcome of there being charge neutral fluxes of electrons and ions striking all surfaces, the former accelerated by the local potential and the ions decelerated by the local potential.

The average electron energy striking surfaces includes both the primary electrons incident onto the surface and secondary electrons produced by the primary electrons. When including SEE, the average energy of electrons incident onto the bottom of the feature is about 40 eV, a decrease of almost 200 eV. This reduction in energy is due to a *dilution* effect from the abundant low-energy SEs that are emitted along the sidewalls that are accelerated toward a more positive portion of the feature. These electrons arrive with the sum of their emission energy (typically several eV) and the

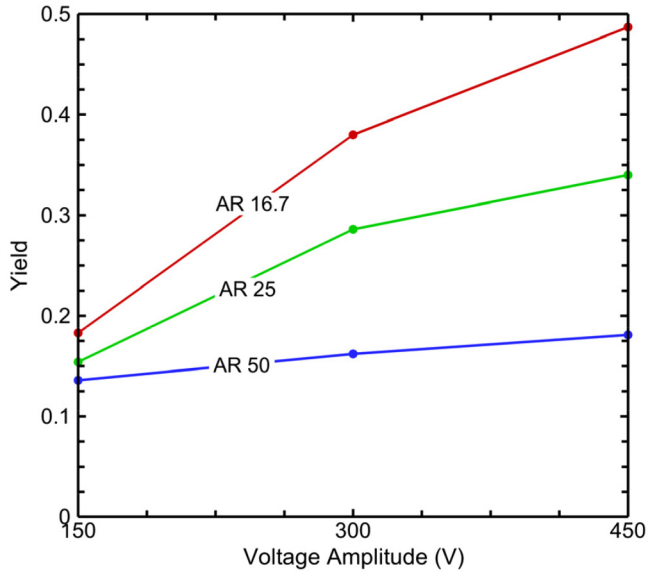


**FIG. 11.** Average secondary electron emission yield as a function of voltage amplitude at ARs of 16.7, 25, and 50.

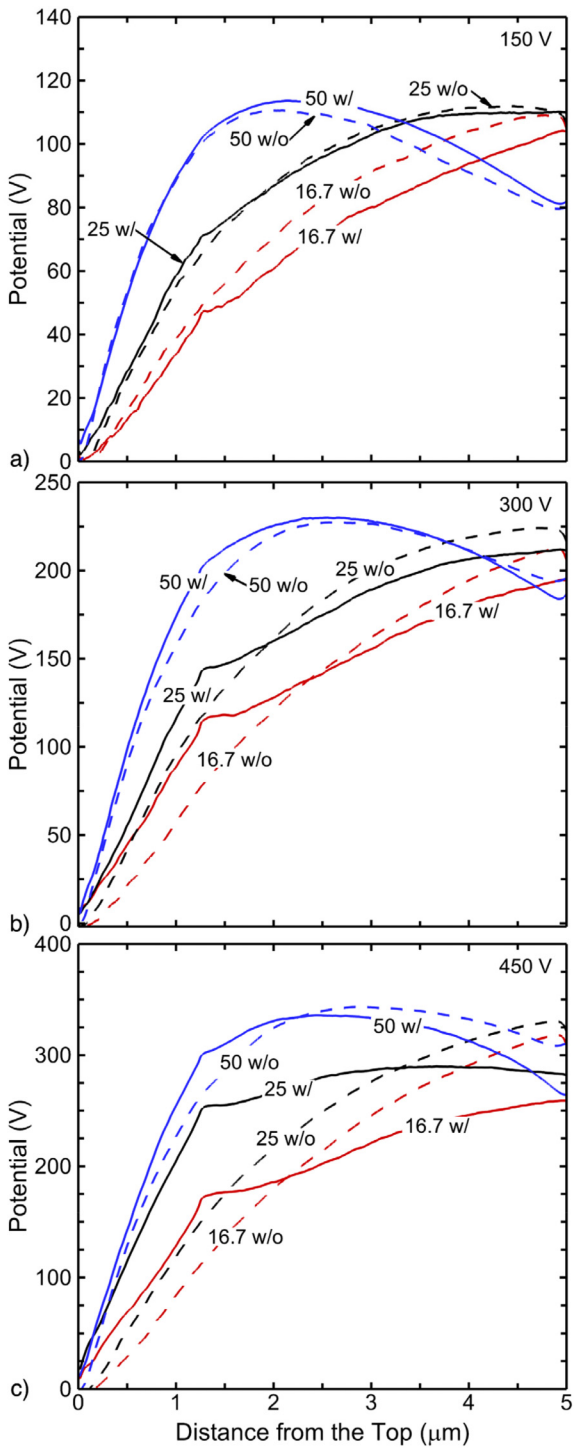


**FIG. 12.** Electric potential distribution along the trench sidewall measured from the trench top for ARs of 16.7, 25, and 50. Values are shown when including SEE (denoted as "w/") and excluding SEE ("w/o"), for voltage amplitudes of (a) 150, (b) 300, and (c) 450 V.

difference in potential between their site of emission and site of collection.

The fluxes of electrons incident onto surfaces near the bottom of the feature significantly increase when including SEE. (These fluxes are of *incident* electrons and are not reduced to reflect the emission of electrons.) The incident primary electrons accelerated into the feature gain enough energy so that their SEY becomes significant, leading to the emission of SEs. These emitted SEs are then accelerated toward the lower portion of the feature, significantly

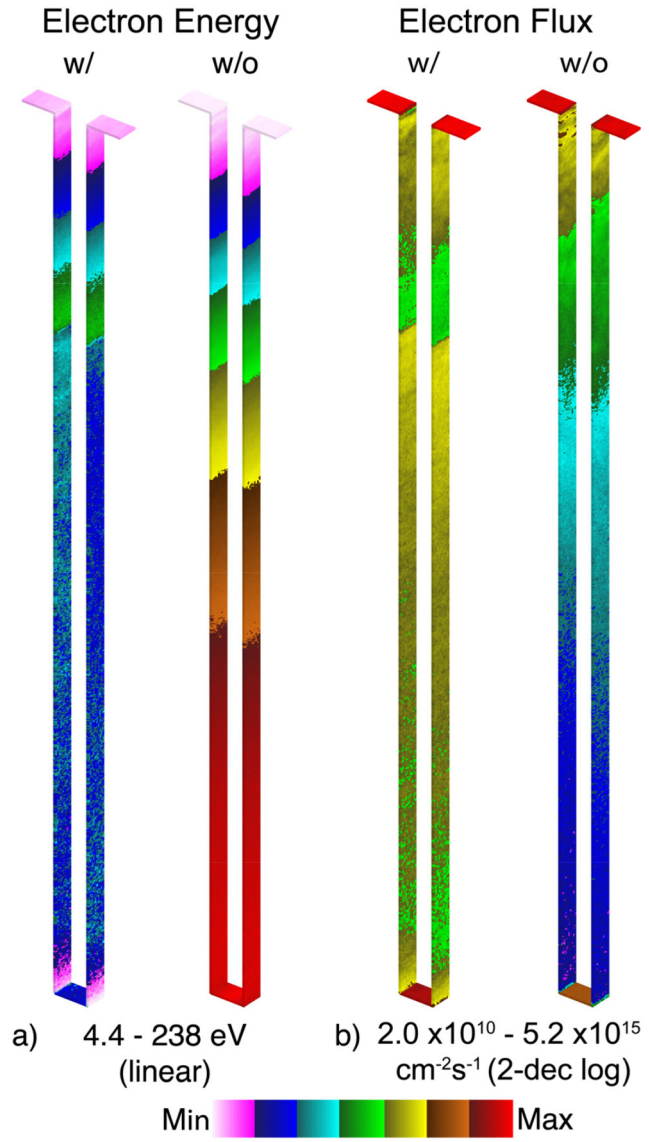


**FIG. 13.** Steady-state distributions of electrons striking surfaces in a feature having an AR of 25 and voltage amplitude of 300 V. (a) Energy and (b) flux of incident electrons. Values are shown when including SEE (denoted as "w/") and excluding SEE ("w/o").

increasing the *incident* electron flux and reducing the average electron energy incident at those locations.

### B. Charging of vias

The steady-state electric potential and the sidewall potential of the predefined via for AR = 20 are shown in Fig. 14 with and without SEE. In the absence of SEE, the vias generally have more sidewall charging, resulting in there being a maximum in potential both on the sidewalls and on the bottom of the feature. Vias have a larger surface-to-volume ratio for the same AR than for a trench, resulting in greater likelihood of charged particles striking sidewalls before the bottom of the feature. Electrons even with a broad angle entering the feature parallel to the sidewalls in a trench will, in the absence of transverse electric fields, eventually strike the bottom of the feature. In vias, electrons entering the feature with an angle larger than the view angle from the bottom of the feature will strike a wall before reaching the bottom.

With SEE, similar but more pronounced trends in reconfiguring charge occur in vias compared to trenches. Including SEE produces a reduction in potential with the degree of reduction increasing with increasing voltage and redistribution of charge. The transient phases of the charging process for vias with and without

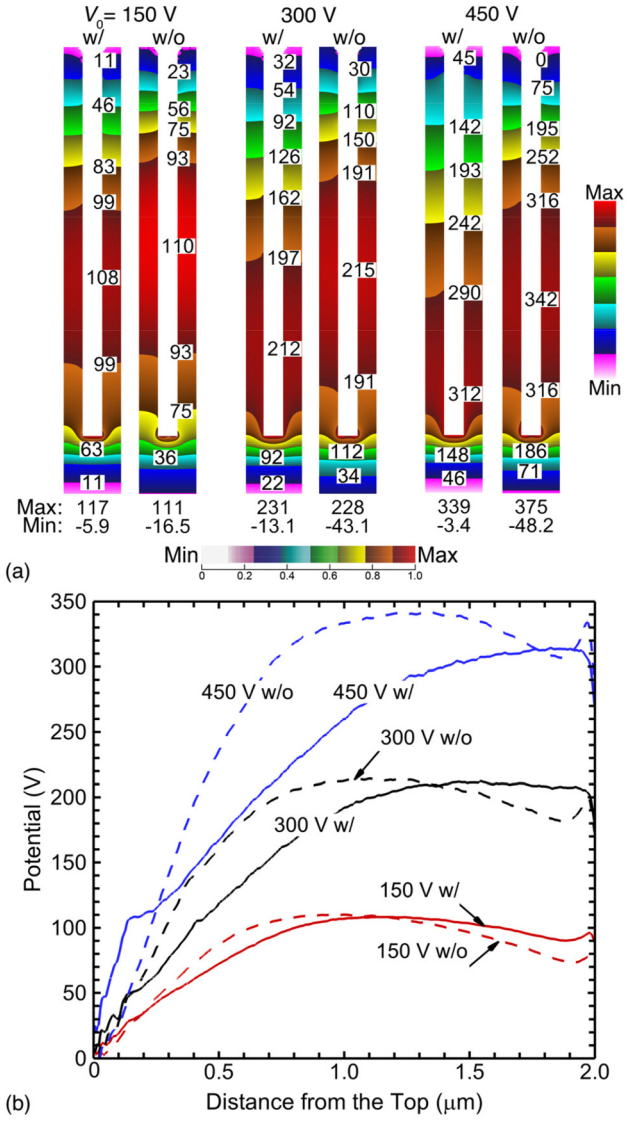


**FIG. 14.** Charging properties of vias with AR = 20 and voltage of $V_0$ = 150, 300, and 450 V with ("w/") and without ("w/o") SEE. (a) Electric potential and (b) electric potential along the sidewall of the via measured from the trench top.

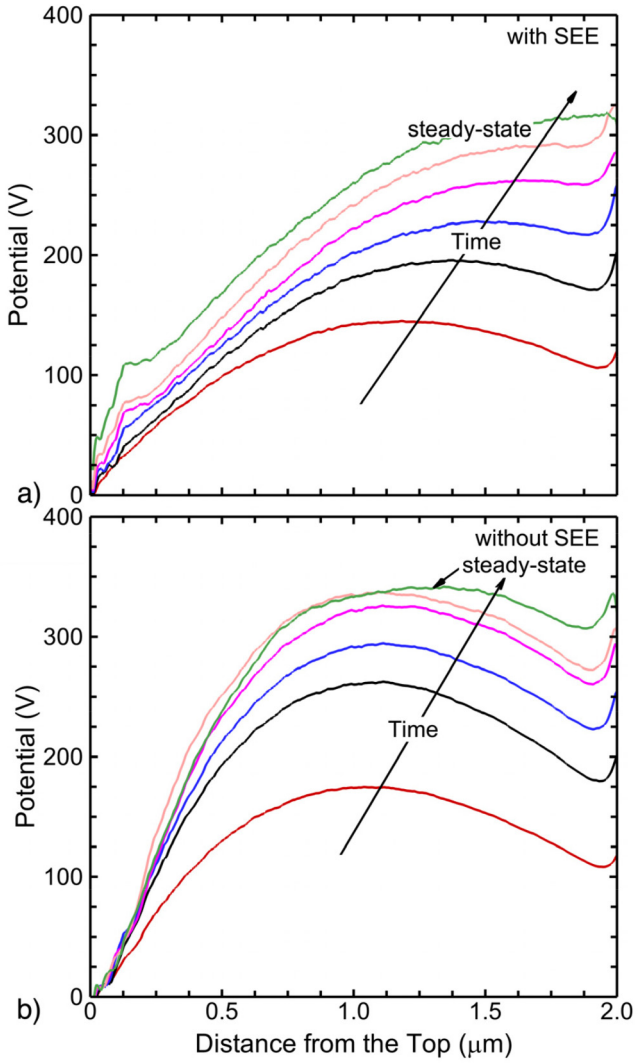


**FIG. 15.** Evolution of electric potential along the sidewall of the via of an AR of 20 (a) with and (b) without SEE for a voltage of 450 V.

SEE are shown in Fig. 15 for AR = 20 by the potential on the sidewall in the approach to the steady state. Without SEE, the potential has a maximum on the sidewalls at midfeature and at the bottom of the feature. This shape is generally preserved in the approach to the steady state. With SEE, the potential initially also has maxima on the sidewalls and bottom of the feature. However, in the steady state, the maximum in potential shifts exclusively to the bottom of the feature due to charge redistribution. With a local maximum in potential initially at midfeature, SEs emitted at the top of the feature will prioritize neutralization of positive charge at midfeature, causing the maximum in potential on the sidewall to shift toward the bottom of the feature.

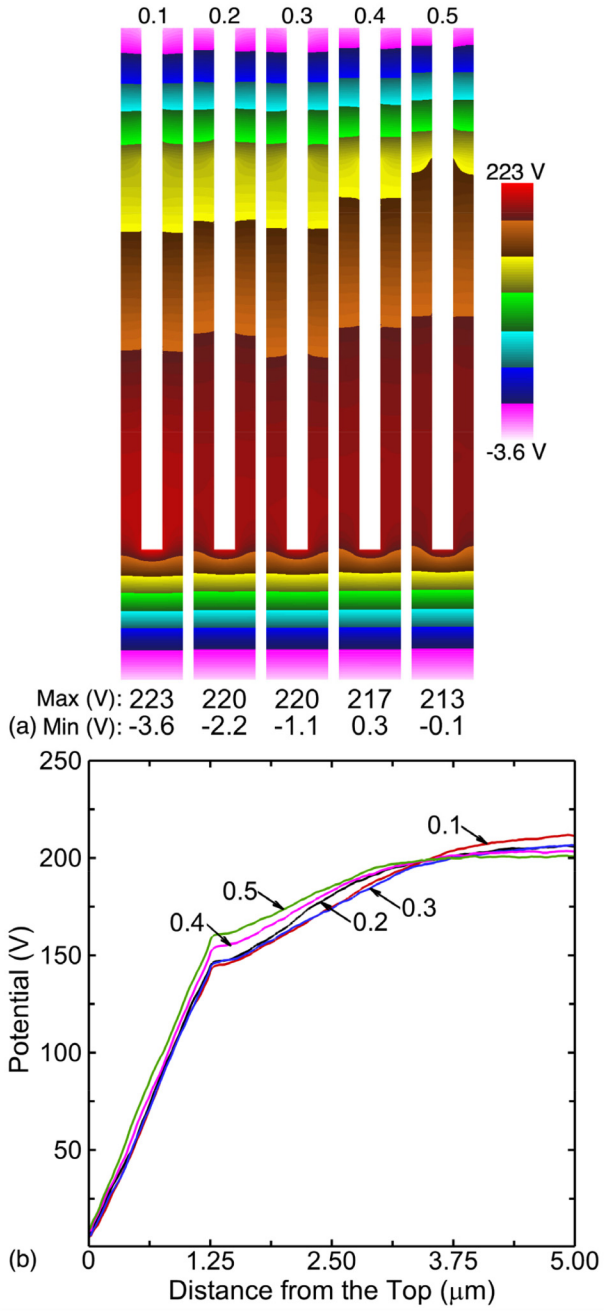


**FIG. 16.** Charging properties for a trench with AR = 25 and $V_0$ = 300 V for ion SEYs of 0.1–0.5. (a) Electric potential profile and (b) electric potential along the trench sidewall.

### C. Significance of ion-induced SEE

The ion-induced SE coefficient for $SiO_2$ was varied from 0.1 to 0.5 to evaluate the significance of ion-induced SEE in charge redistribution. The trench feature has AR = 25, and the voltage is $V_o$ = 300 V. The steady-state electric potential distributions and the potentials along the sidewall are shown in Fig. 16 although the changes are not large. The electric potential is most positive at the bottom of the trench for all SEY. As the ion-induced SEY increases, there is a small decrease in the global maximum of potential, 223–213 V. Higher in the feature the potential has a corresponding increase of 15 V.

The electric potential distribution profile is related to the energy and incident angle of the charged particles. While the most energetic ions with small angular spread are able to reach the bottom of the feature, less energetic ions with larger incident angles strike the upper surfaces of the trench. Secondary emission from the higher portions of the feature generates electrons, which are accelerated deeper into the feature, increasing potential in the upper portion of the feature and decreasing potential lower in the feature. That said, these changes potential with changes in ion SEY are not large. Redistribution of charge is dominated by electron-induced SEE. There are systematic trends in potential with the change in SEY. The statistical nature of the Monte Carlo simulation produces some oscillation in the computed potential. The oscillation in the maximum potential can be as large as 10–15 V in the steady-state. The difference in potential produced by varying the ion-induced SEY does not greatly exceed this maximum in the statistical variation. The conclusion is that ion-impact SEE, at least at these ion energies, is not the major contributor to charge redistribution and that charge redistribution is dominated by electron-impact secondary emission.

### D. Effect of anisotropic electrons on charging

Electric field reversals adjacent to the sheath can produce EEADs with higher energies and narrower angular distributions compared to thermal incident electrons. One of the original motivations for VWT was to produce electric field reversals to craft EEADs that are better able to penetrate deeply into features to neutralizing positive charge. Comparisons of feature charging between VWT produced EEADs and thermal electron distributions were made for the AR = 25 predefined trench. This comparison was conducted by computing IEADs and EEADs using VWT and using those EADs to predict feature potential. Using the same magnitude of fluxes and IEADs, the EEAD was then replaced by a synthetic Maxwellian distribution having an electron temperature of 3 eV (denoted as ThermE). Feature charging was then predicted with the ThermE conditions.

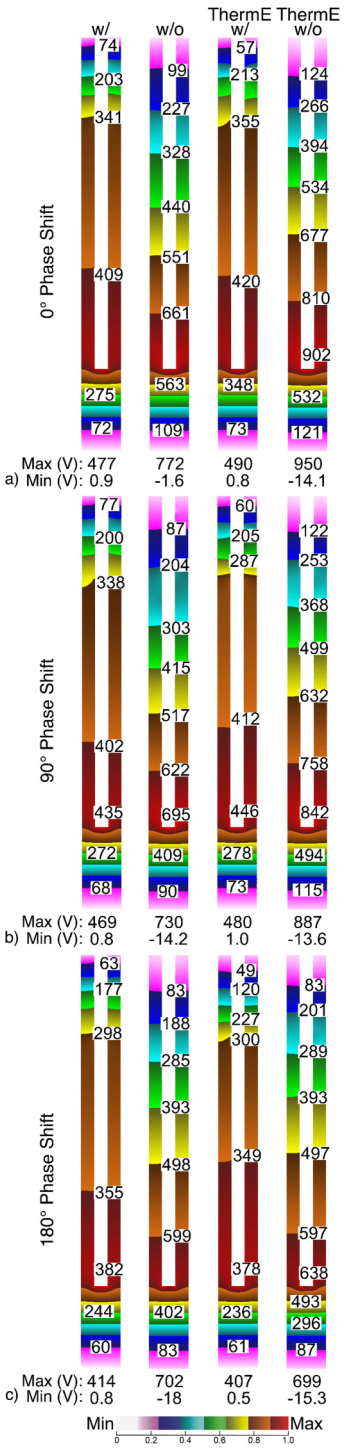


**FIG. 17.** Electric potential profiles using voltage-waveform tailoring at (a) $\varphi_{2,4} = 0°$, (b) 90°, and (c) 180° with SEE and without SEE. Comparisons are made to electron fluxes having a synthetic thermal EEAD with $T_e = 3$ eV with SEE (ThermE w/ SEE) and without SEE (ThermE w/o SEE).

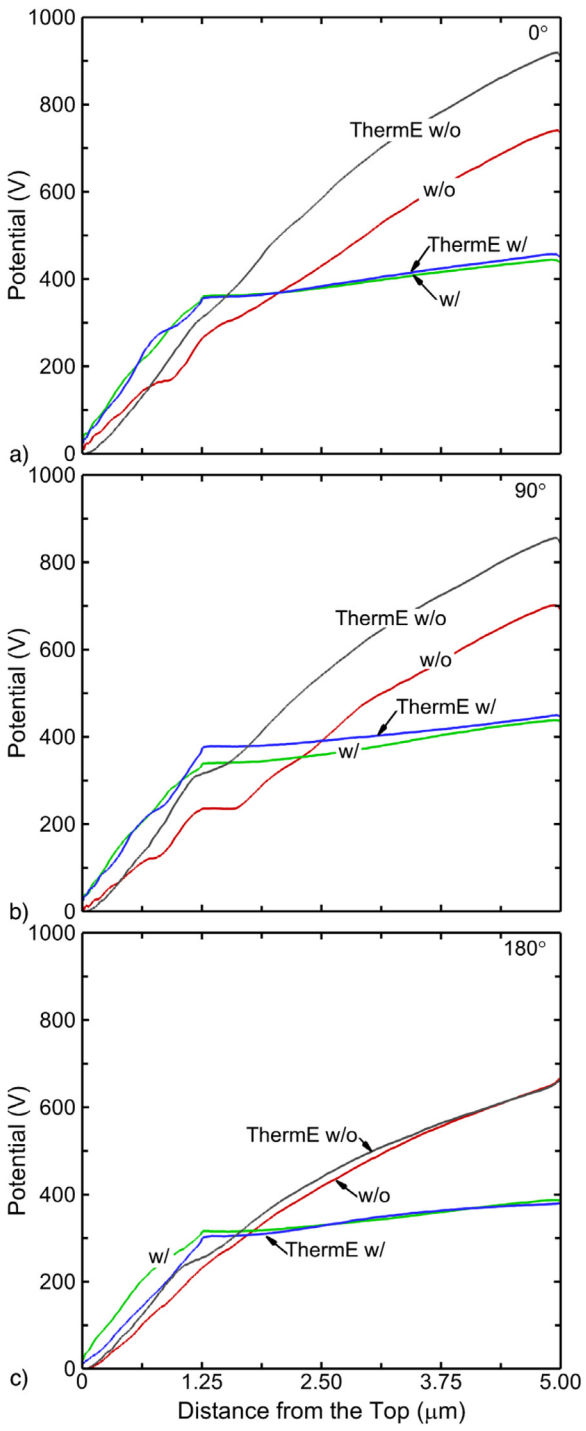


**FIG. 18.** Electric potential along the sidewall of trenches using voltage-waveform tailoring for (a) $\varphi_{2,4} = 0°$, (b) 90°, and (c) 180° (bottom). Values when using EADs produced by VWT with SEE ("w/") and without SEE ("w/o") are compared with cases using the original IEAD along with synthetic thermal EEAD with $T_e = 3$ eV with SEE ("ThermE w/)" and without SEE ("ThermE w/o").

The steady-state potentials are shown in Fig. 17 for EEADs produced with $\varphi_{2,4}$ varied between 0°, 90°, and 180° with and without SEE. These results are compared to cases for electron fluxes having thermal EEADs. The electric potentials along the sidewall for these cases are in Fig. 18. The reduction in electric potential due to charge redistribution with SEE occurs across all phase shifts. The maximum in potential decreases by about 40% across all phase shifts.

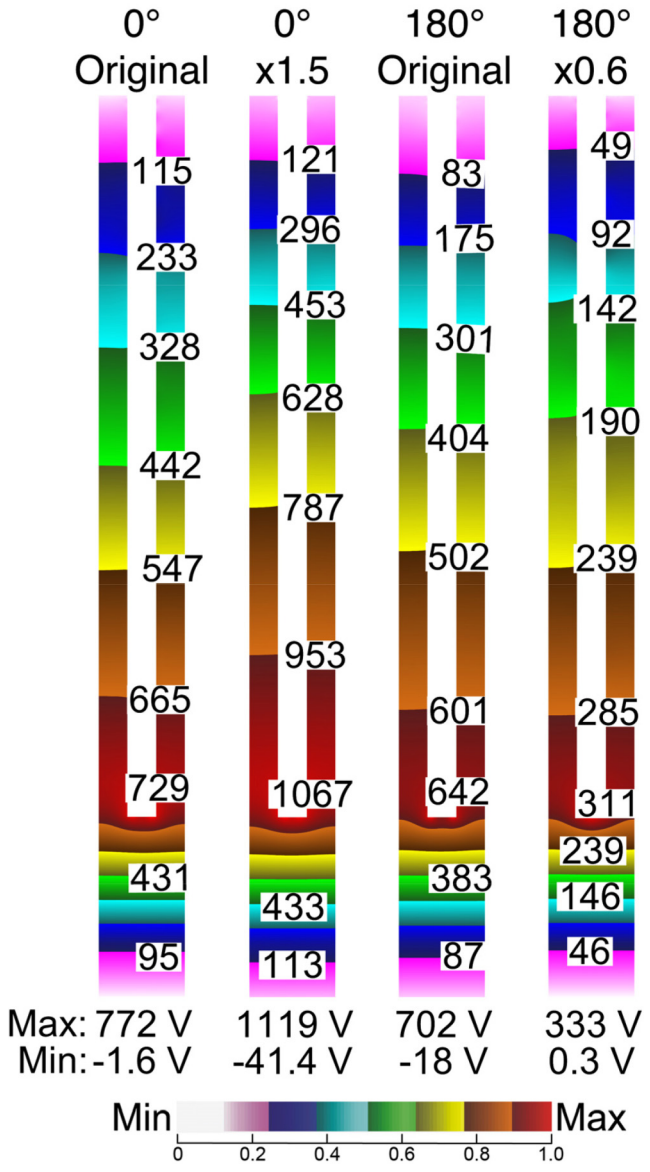


**FIG. 19.** Electric potential profiles of trenches without SEE using voltage-waveform tailoring at $\varphi_{2,4} = 0°$ and 180°. The EEADs at $\varphi_{2,4} = 0°$ are broadened by a factor of 1.5 (denoted as "×1.5"), and the EEADs at $\varphi_{2,4} = 180°$ are narrowed by a factor of 0.6 (as "×0.6").

Previous research has shown that VWT produced EEADs can more readily neutralize positive charging at the bottom of features due to its anisotropy.[8] In the absence of SEE, as shown in Fig. 18, anisotropic electrons, indeed, reduce the maximum electric potential by 178 and 157 V at $\varphi_{2,4} = 0°$ and 90° phase shifts, respectively, compared to thermal EEADs. However, at $\varphi_{2,4} = 180°$, the maximum electric potential changes little between thermal and anisotropic electrons fluxes even though electrons at $\varphi_{2,4} = 180°$ have higher energy compared to thermal electrons (see Fig. 10). The energy with which electrons strike the feature is the sum of their incident energy and the energy gained by acceleration from the positive potential in the feature. With the in-feature potential being 400–500 V and the electron energy for $\varphi_{2,4} = 180°$ being only 10–20 V, the majority of the electron energy is due to acceleration by the positive charge, which applies equally to the thermal electrons.

When SEE is included, the impact on the potential of using anisotropic versus thermal becomes much smaller, as shown in Fig. 18. $\varphi_{2,4} = 0°$ and 90° cases with anisotropic electrons exhibit slightly less positive potential compared to the corresponding cases with thermal electrons, while the $\varphi_{2,4} = 180°$ case shows an almost identical potential along the sidewall in the $SiO_2$ region. Conditions that produce large fluxes of SEs result in charge redistribution being a dominant factor in reducing potential. As a result, with SEE, the anisotropy of the primary electrons is less important in charge mitigation.

The angular width of the EEAD is also a factor in feature charging. To demonstrate this dependence, the EEAD at $\varphi_{2,4} = 0°$ phase shift without SEE was broadened by a factor of 1.5, and the EEAD at $\varphi_{2,4} = 180°$ without SEE was narrowed to 0.6 times its original width. The corresponding steady-state charging potentials are in Fig. 19. With the broadened EEAD, the maximum potential at 0° phase shift increases by 45%. Conversely, with the narrowed EEAD, the peak potential at 180° phase shift decreases by 49%. These results suggest that controlling the lateral component of the electron velocity distribution is key to mitigating charging since the energy of the electrons striking the inside of the feature is usually dominated by acceleration by the positive charge. A narrower angular distribution enables a larger fraction of the incident electron flux to be naturally accelerated by positive potential to neutralize charge deeper in the feature.

## VI. CONCLUDING REMARKS

The consequences of SEE on dynamic and steady-state charging of HAR features in CCP systems were investigated for the plasma properties of a single frequency CCP system sustained in pure argon at 10 mTorr for voltage amplitudes of 150 to 450 V at 20 MHz. The steady-state electric potential profiles of a predefined trench with an AR of 16.7–50 and a predefined via with an AR of 20 were computed.

The maximum electric potential was found to correlate with bias voltage amplitude in both trench and via features and inversely with the AR of the feature in trench features. With SEE, there was charge redistribution in the feature by a net transfer of negative charge from less positive regions of the feature receiving larger primary electron fluxes (typically in the upper portion of the

feature) to more positive regions receiving smaller primary electron fluxes (typically in the lower portion of the feature). As the degree of charge redistribution increased, the global maximum in electric potential decreased compared to the absence of SEE with the upper region becoming slightly more positively charged. The ion-induced SEY was nearly constant at 0.10 for the range of ion energies considered here while electron-induced SEY scales with incident energy and peaks at a few hundred eV. The degree of charge redistribution correlates with the positive electric potential, which accelerates electrons into the feature, thereby increasing the electron-induced SEY. The degree of charge redistribution correlates inversely with the AR. Higher AR and narrower features spatially confine the SEs and the distance over which charge can be redistributed. The charge redistribution alters the electric potential profile within the feature. The general trend is a shifting of positive potential to lower in the feature.

The effectiveness of VWT for charging remediation was evaluated with and without SEE. VWT produces electron fluxes onto the wafer having energies exceeding 100 eV and angular spreads as low a 5°–10° depending on the phase shift $\varphi_{2,4}$. Electric potentials obtained with EEADs using VWT were compared with those produced by synthetic EEADs consisting of thermal electrons with electron temperature $T_e = 3$ eV. When SEE is excluded, EEADs produced with VWT effectively mitigate charging compared to thermal distributions. However, with SEE, charge redistribution dominates the neutralization of positive potential and the additional potential reduction occurring with anisotropic electrons becomes less important.

Due to their large secondary emission coefficients, high-energy secondary and bulk electrons have a disproportionate influence on feature charging. These high-energy electrons are also capable of stimulating etching and deposition of materials, and cross-linking (hardening) of polymer photoresists.[49] For example, Lin *et al.* showed that combining a remote plasma source and an electron beam (<1000 eV) can etch $SiO_2$ in a self-limiting manner.[50] Li *et al.* demonstrated the selective etching of Ru and Ta in a combined remote plasma source and electron beam system.[51] In this investigation, we showed that electrons, both primary and secondary, can gain hundreds of eV in addition to their initial energy after being accelerated by the in-feature electric potential. These incident energies are commensurate with the energy of deliberately applied electron beams for deposition and etching. By analogy, one might expect that these high energy electron fluxes are also capable of stimulating etching or deposition reactions or creating free-radical sites that would lower the energy barrier for reactions.

Quantitative validation of the trends in charging discussed here would require high-precision, time dependent measurements of electric potential performed inside HAR features having dimensions of industrial interest. Given that these measurements would be challenging, less direct validation might be achieved through rare-gas, HAR physical sputtering of materials having very different, but well known, secondary electron yields. Given that rates of physical sputtering are well known for a given IEAD, deviations from expected behavior for materials having, for example, very low or high SEY, could be attributed to the differences in in-feature charging due to those different SEYs.

Although it is not addressed in this paper, the characteristics of the emission site of SEs are likely important to charge redistribution. The simulations discussed in this paper assumed smooth surfaces on any given voxel, which limits roughness to the order of a few nm. SEY coefficients depended only on incident particle energies and angles for a given material. Surface roughness on spatial scales less than addressed here may produce local electric field enhancement that in turn will affect SEY coefficients. We assumed here that SEE occurred at the site of the incident particle, whereas high-energy electrons can implant with secondary electron emission occurring in the local vicinity. With material properties varying on the order of nm to tens of nm, the nonlocal emission of secondary electrons could influence redistribution of charge and the in-feature potential. Particularly important to HAR etching, which is performed with ions having energies sometimes exceeded several keV, is the formation of mixed surface layers. These mixed layers will likely have different secondary electron yields, thermal and electric conductivities, and permittivities compared to the initial pure materials. Although the change in physical properties of mixed layers is usually accounted for in profile simulations, addressing the change in the secondary electron yield should also be addressed.

## ACKNOWLEDGMENTS

This work was supported by the Department of Energy Office of Fusion Energy Sciences under Award No. DE-SC0024545 and Samsung Electronics, Ltd.

## AUTHOR DECLARATIONS

### Conflict of Interest

The authors have no conflicts to disclose.

### Author Contributions

**Chenyao Huang:** Formal analysis (lead); Methodology (lead); Software (lead); Visualization (lead); Writing – original draft (lead); Writing – review & editing (equal). **Mark J. Kushner:** Conceptualization (lead); Funding acquisition (lead); Project administration (lead); Writing – review & editing (equal).

## DATA AVAILABILITY

The data that support the findings of this study are available from the corresponding author upon reasonable request.

## REFERENCES

[1]H. Tanaka, M. Kido, K. Yahashi, M. Oomura, R. Katsumata, and M. Kito, in *2007 IEEE Symposium on VLSI Technology*, Kyoto, Japan, 12–14 June 2007 (IEEE, Piscataway, NJ, 2007), pp. 14–15.
[2]P. Feng *et al.*, IEEE Electron Device Lett. **38**, 1657 (2017).
[3]Y. Li, IEEE Solid State Circuits Mag. **12**, 56 (2020).
[4]V. M. Donnelly and A. Kornblit, J. Vac. Sci. Technol. A **31**, 50825 (2013).
[5]J. Matsui, K. Maeshige, and T. Makabe, J. Phys. D: Appl. Phys. **34**, 2950 (2001).
[6]G. S. Hwang and K. P. Giapis, J. Appl. Phys. **82**, 566 (1997).
[7]S. N. Hsiao, M. Sekine, K. Ishikawa, Y. Iijima, Y. Ohya, and M. Hori, Appl. Phys. Lett. **123**, 212106 (2023).

[8]F. Krüger, H. Lee, S. K. Nam, and M. J. Kushner, J. Vac. Sci. Technol. A **41**, 13006 (2023).
[9]S. L. Lai, D. Johnson, and R. Westerman, J. Vac. Sci. Technol. A **24**, 1283 (2006).
[10]S. N. Hsiao, M. Sekine, Y. Iijima, and M. Hori, Chem. Mater. **36**, 11042 (2024).
[11]Y. Kihara, M. Tomura, W. Sakamoto, M. Honda, and M. Kojima, in *2023 IEEE Symposium on VLSI Technology and Circuits (VLSI Technology and Circuits)*, Kyoto, Japan, 11–16 June 2023 (IEEE, Piscataway, NJ, 2023), pp. 1–2.
[12]B. Wu, A. Kumar, and S. Pamarthy, J. Appl. Phys. **108**, 51101 (2010).
[13]C. Han, Z. Wu, C. Yang, L. Xie, B. Xu, L. Liu, Z. Yin, L. Jin, and Z. Huo, Semicond. Sci. Technol. **35**, 045003 (2020).
[14]D. J. Economou, J. Phys. D: Appl. Phys. **47**, 303001 (2014).
[15]A. Ranjan, V. M. Donnelly, and D. J. Economou, J. Vac. Sci. Technol. A **24**, 1839 (2006).
[16]D. J. Economou, Appl. Surf. Sci. **253**, 6672 (2007).
[17]T. Ohmori and T. Makabe, Appl. Surf. Sci. **254**, 3696 (2008).
[18]B. Jinnai, T. Orita, M. Konishi, J. Hashimoto, Y. Ichihashi, A. Nishitani, S. Kadomura, H. Ohtake, and S. Samukawa, J. Vac. Sci. Technol. B **25**, 1808 (2007).
[19]Y. Zhai, R. Ge, Z. Hu, J. Li, H. Shao, J. Cheng, L. Filipovic, and R. Chen, J. Appl. Phys. **137**, 63302 (2025).
[20]J. E. Yater, J. Appl. Phys. **133**, 050901 (2023).
[21]L. Reimer, *Scanning Electron Microscopy* (Springer, Berlin, 1998), p. 135, Chap. IV.
[22]M. S. Chung and T. E. Everhart, J. Appl. Phys. **45**, 707 (1974).
[23]A. P. Palov, Y. A. Mankelevich, T. V. Rakhimova, and D. Shamiryan, J. Phys. D: Appl. Phys. **43**, 075203 (2010).
[24]J. Burns, Phys. Rev. **119**, 102 (1960).
[25]E. Giglio and T. Le Cornu, Phys. Rev. A **103**, 032825 (2021).
[26]D. C. Joy, M. S. Prasad, and H. M. Meyer, J. Microsc. **215**, 77 (2004).
[27]A. Shih, J. Yater, C. Hor, and R. H. Abrams, IEEE Trans. Electron Devices **41**, 2448 (1994).
[28]M. J. Kushner, J. Phys. D: Appl. Phys. **42**, 194013 (2009).
[29]C. Qu, S. K. Nam, and M. J. Kushner, Plasma Sources Sci. Technol. **29**, 085006 (2020).
[30]S. H. Song and M. J. Kushner, Plasma Sources Sci. Technol. **21**, 055028 (2012).
[31]A. V. Vasenkov, X. Li, G. S. Oehrlein, and M. J. Kushner, J. Vac. Sci. Technol. A **22**, 511 (2004).
[32]P. Tian and M. J. Kushner, Plasma Sources Sci. Technol. **24**, 034017 (2015).
[33]C. M. Huard, Y. Zhang, S. Sriraman, A. Paterson, and M. J. Kushner, J. Vac. Sci. Technol. A **35**, 031306 (2017).
[34]S. Huang, S. Shim, S. K. Nam, and M. J. Kushner, J. Vac. Sci. Technol. A **38**, 23001 (2020).
[35]A. V. Phelps and Z. L. Petrovic, Plasma Sources Sci. Technol. **8**, R21 (1999).
[36]A. Bogaerts and R. Gijbels, Plasma Sources Sci. Technol. **11**, 27 (2002).
[37]K. Ohya and J. Kawata, Nucl. Instrum. Methods Phys. Res. B **90**, 552 (1994).
[38]U. V. Gemmingen, Surf. Sci. **120**, 334 (1982).
[39]Y. Susuki, T. Baba, S. Fukui, and M. Mannami, Surf. Sci. **254**, 97 (1991).
[40]V. Castaldo, J. Withagen, C. Hagen, P. Kruit, and E. Van Veldhoven, Microsc. Microanal. **17**, 624 (2011).
[41]E. J. Sternglass, Phys. Rev. **108**, 1 (1957).
[42]Y. Yamamura, C. Mössner, and H. Oechsner, Radiat. Eff. **103**, 25 (1987).
[43]J. Fernandez-Coppel, R. Wirz, and J. Marian, J. Appl. Phys. **135**, 83301 (2024).
[44]M. A. Furman and M. T. F. Pivi, Phys. Rev. Spec. Top. Accel. Beams **5**, 124404 (2002).
[45]C. K. Purvis, NASA Technical Memorandum (1979), p. 79299.
[46]M. J. Mandell, P. R. Stannard, and I. Katz, NASCAP Programmer's Reference Manual, NASA Contractor Report (1993).
[47]H. Jahrreiss and W. Oppel, J. Vac. Sci. Technol. **9**, 173 (1972).
[48]Z. J. Ding, H. M. Li, R. Shimizu, and K. Goto, J. Surf. Anal. **15**, 186 (2008).
[49]S. J. Randolph, J. D. Fowlkes, and P. D. Rack, Crit. Rev. Solid State Mater. Sci. **31**, 55 (2006).
[50]K. Y. Lin, C. Preischl, C. F. Hermanns, D. Rhinow, H. M. Solowan, M. Budach, K. Edinger, and G. S. Oehrlein, J. Vac. Sci. Technol. A **40**, 063004 (2022).
[51]Y. Li, H. Marbach, C. Preischl, M. Budach, D. Rhinow, K. Edinger, and G. S. Oehrlein, J. Vac. Sci. Technol. A **43**, 013004 (2025).